Vol. 20, No. 2 (2021) 911-940
Revista Mexicana de Ingeniería Química

Multiscale modeling of a membrane bioreactor for the treatment of oil and grease rendering wastewaters

Modelado multiescala de un biorreactor de membrana para el tratamiento de aguas residuales con grasas y aceites

J. Sánchez-Vargas[1] and F.J. Valdés-Parada[2]*

[1] *Unidad de Investigación Médica en Inmunoquímica, Hospital de Especialidades, Centro Médico Nacional Siglo XXI, Instituto Mexicano del Seguro Social, Ciudad de México, México.*
[2] *Departamento de Ingeniería de Procesos e Hidráulica. División de Ciencias Básicas e Ingeniería, Universidad Autónoma Metropolitana-Iztapalapa, Ciudad de México, México.*

Received: February 14, 2021; Accepted: March 17, 2021

Abstract

Membrane bioreactors represent an attractive alternative for food industries wastewater treatment. This type of reactors comprise an aerobic tank (where the biochemical reactions take place) and a membrane tank (where the final filtration process occurs). Mathematical modeling of these systems is a practical tool for the design, control and optimization of wastewater treatment plants. Among the modeling approaches, there is no mathematical model that is specifically designed for membrane bioreactors, and that captures the hierarchical nature of these systems. In the present work, new mathematical models for mass and momentum transport are derived from the fundamental equations at the continuum level. With the use of the volume averaging method, effective medium models for both the aerobic and membrane tanks were developed. This modeling approach has the advantage that the coefficients involved in the model can be predicted from closure schemes, without representing a demanding computational effort. This deterministic model allows predicting the most favorable design and operating conditions. Additionally, numerical simulations of these models give rise to a better understanding of the involved mass transport mechanisms in the membrane tank, this is achieved through the prediction of the fluid velocity, and the dynamics of the total mass flux and the concentration at each point in the tank. The models derived here are valuable because they allow analyzing the effect of each (operational and/or design) parameter over the dynamics of long-chain fatty acids and oxygen concentrations.

Keywords: membrane bioreactor, mathematical modeling, upscaling, mass and momentum transport, numerical simulations.

Resumen

Los biorreactores de membrana representan una alternativa atractiva para el tratamiento de aguas residuales de industrias alimentarias. Este tipo de reactores se componen de un tanque aerobio (donde las reacciones bioquímicas tienen lugar) y un tanque de membrana (donde el proceso de filtración final ocurre). El modelado matemático de estos sistemas es una herramienta práctica para el diseño, control y optimización de plantas de tratamiento. Entre los enfoques de modelado no existe un modelo matemático cuyo diseño sea específico para biorreactores de membrana, y que capture la naturaleza jerárquica de estos sistemas. En este trabajo, nuevos modelos matemáticos para el transporte de masa y cantidad de movimiento se deducen a partir de las ecuaciones fundamentales al nivel de escala del continuo. Mediante el uso del método del promedio volumétrico, se deducen modelos de medio efectivo tanto para el tanque aerobio como para el tanque de membrana. Este enfoque de modelado tiene la ventaja de que los coeficientes involucrados en el modelo pueden ser predichos a partir de esquemas de cerradura, sin ser su solución computacionalmente demandante. Este modelo determinista permite predecir las condiciones de diseño y operación más ventajosas. Adicionalmente, las simulaciones numéricas de los modelos dan lugar al mejor entendimiento de los mecanismos de transporte de masa involucrados en el tanque de membrana, esto se logra mediante la predicción de la velocidad del fluido, y de la dinámica del flux total de masa y de la concentración en cada punto del tanque. Los modelos deducidos aquí son valiosos porque permiten analizar el efecto de cada parámetro (operativo y / o de diseño) sobre la dinámica de los ácidos grasos de cadena larga y la concentración de oxígeno.

Palabras clave: biorreactor de membrana, modelado matemático, escalamiento, transporte de masa y cantidad de movimiento, simulaciones numéricas.

---

* *Corresponding author. E-mail*: `iqfv@xanum.uam.mx`

https://doi.org/10.24275/rmiq/Fen2368
ISSN:1665-2738, *issn-e*: 2395-8472

1 Introduction

A membrane bioreactor (MBR) is a wastewater treatment system, consisting of a biological degradation compartment and a physical separation tank through membrane filtration. These bioreactors have been successfully implemented for both municipal and industrial wastewater treatment (Asif et al., 2019). In recent years, research articles and patent publications, along with start-ups of treatment plants that use MBRs, show a marked and exponential growth (Krzeminski, Leverette, Malamis, & Katsou, 2017; Xiao, Liang, Wang, Chen, & Huang, 2019). The increasing application of MBRs motivates the development of mathematical models in order to predict mass and momentum transport in these reactors (Rittmann et al., 2018). In addition, mathematical models are desirable because they allow optimization, design and operation of treatment plants, as well as determination of the operational limits of existing facilities (Brannock, Leslie, Wang, & Buetehorn, 2010; Hamedi, Ehteshami, Mirbagheri, Rasouli, & Zendehboudi, 2019). Furthermore, predictive models (*i.e.*, *a priori* models, see Valdés Parada, 2014) have the advantage of not requiring the physical existence of the system under study (Zarragoitia-González, Schetrite, Alliet, Jáuregui-Haza, & Albasi, 2008). Mathematical modeling of wastewater treatment processes is an acceptable and practical tool that is widely used by consulting companies and regulatory agencies (Morgenroth, Arvin, & Vanrolleghem, 2002).

For MBRs, there are two main approaches to system modeling. The first one are the activated sludge models (ASM). These mechanistic and observational models are widely used since the creation of the AMS1 (Henze, Grady, Gujer, Marais, & Matsuo, 1987). These models attempt to represent the biochemical transformations in activated sludge systems through various simplified processes descriptions, based on the mass and momentum transport dynamics observed in wastewater treatment plants (*i.e.*, *a posteriori* modeling) (Hauduc et al., 2012). The use of these models requires knowledge of multiple parameters that are constrained to specific operating conditions (Jeppsson, 1996). Although ASMs were developed for conventional activated sludge systems, several authors suggest that they could be used to model biomass kinetics in MBRs systems (d'Antonio, Esposito, Fabbricino, & Panico, 2016; Janus & Ulanicki, 2016; Lee, Cho, Seo, Lee, & Ahn, 2002; Lu et al., 2001; Maere, Verrecht, Moerenhout, Judd, & Nopens, 2011; Tenore, Vieira, Frunzo, Luongo, & Fabbricino, 2018). This is because the MBR system is considered as an activated sludge in which the secondary clarifier was replaced by a membrane filtration unit. The principal alternatives for modeling an MBR with an ASM is the addition of submodels (Fenu et al., 2010). Nevertheless, the extension of these models entails the introduction of a considerable number of additional parameters, leading to an overparameterization problem (Takács et al., 2011), thus limiting their practical application to MBRs.

The second approach are the computational fluid dynamics (CFD) models. These are based on the conservation laws (for mass, momentum and mechanical energy) that govern fluid mechanics at the continuum scale (Hu, 2012), and involve demanding numerical simulations (Xiea et al., 2016). In order to perform these simulations, using for instance finite elements or finite volume methods, high-resolution computational meshes are required, especially in the fibers interior that make up ultrafiltration cassettes (Saalbach & Hunze, 2008). This issue, along with the requirement of having moving meshes to describe air bubbles dynamics, restricts the applicability of CFD models in wastewater treatment plants, as considerable computational efforts are required. Furthermore, CFD serves primarily to model fluid flow and, in many cases, nutrient transport and reaction in MBRs is modeled coupling an ASM (Janus & Ulanicki, 2016; Mannina, Cosenza, & Ekama, 2018).

The above shows the relevance and need of developing mathematical models specific to MBRs. Due to the hierarchical nature of the system, it is desirable that these models are applicable at the reactor scale level, but they should also be capable of capturing the essential information from the microscale. Consequently, the objective of this work is the derivation of mathematical models for the MBR system by means of an upscaling approach, based upon the volume averaging method. In this context, *upscaling* is used to denote the systematic filtering of information when going from a certain scale level to a superior one. Once the models are derived, they are used to determine the most favorable design and operation conditions for the degradation of oil and grease substrates (represented as long-chain fatty acids). These contributions are relevant for future experimental works, both for design activities and for the proposition of improvements to existing systems. In order to accomplish these goals, the work is organized as follows: Firstly, the system components are briefly described in section 2 and the two tanks under study and their functions and components are clearly identified. Later on, in sections 3 and 4, the mathematical models for the aerobic tank and the membrane tank are derived, respectively. With these models available, the attention is then directed to the parametric analysis in each tank by means of the numerical solutions of the models as shown in sections 5 and 6, respectively. The outcome of these analyses is the determination of the most favorable design and operation conditions for the system. Finally, the corresponding concluding remarks are reported.

2 System description

Consider a membrane bioreactor with two main tanks connected in series: an aerobic activated sludge reaction tank (from here on, the *aerobic tank*), and a membrane tank with submerged hollow fibre filtration cassettes (in the following, the *membrane tank*). The reactor feed is assumed to consist of wastewater from the food industry that has already undergone a pretreatment process. This wastewater contains oils and greases (*i.e.*, λ-phase), free long-chain fatty acids (LCFA), a liquid phase (β-phase), inert solids and organic matter. The proposed oil and grease concentration in the inflow of aerobic tank is approximately equal to 1.47 g L^{-1} (Acharya, Nakhla, & Bassi, 2006a, 2006b; Kurian, Acharya, Nakhla, & Bassi, 2005; Liu, Nakhla, Bassi, & Al-Sabawi, 2003; Nakhla, Liu, & Bassi, 2006). In the aerobic tank, shown in figure 1, the oil phase is completely degraded through consecutive hydrolysis reaction steps taking place at the boundary between this phase and the liquid region (the η-region), generating free LCFA such as oleic, palmitic and stearic acids (species-A). Therefore, species-A is no longer considered as oil droplets, but as a diluted chemical species everywhere in the system. In this context, the term *region* is used to denote a portion of the system containing more than one phase. The term *zone* is used hereafter to refer indistinctly to a phase or a region. The oxidation reactions of the LCFA take place within the biomass contained in flocs (the ω-region) of different sizes. Oxygen (species-B), is provided through air (the γ-phase) diffusers, located at the bottom of the tank that also promote mixing inside the tank. The diffusers are assumed to have holes with diameters of millimeters, in order to favor mass transport. Both species are consumed inside the flocs, and the excess exits the tank with the effluent. This current becomes the influent of the membrane tank, sketched in figure 2, where the filtration process occurs, yielding a permeate current of treated water (the β-phase). The membrane tank is also aerated by diffusers located below the filtration cassettes (the ζ-region), with the purpose of removing fouling materials from the membrane surface. A cassette is a membrane modules assembly, where the combine permeate is collected in the upper section.

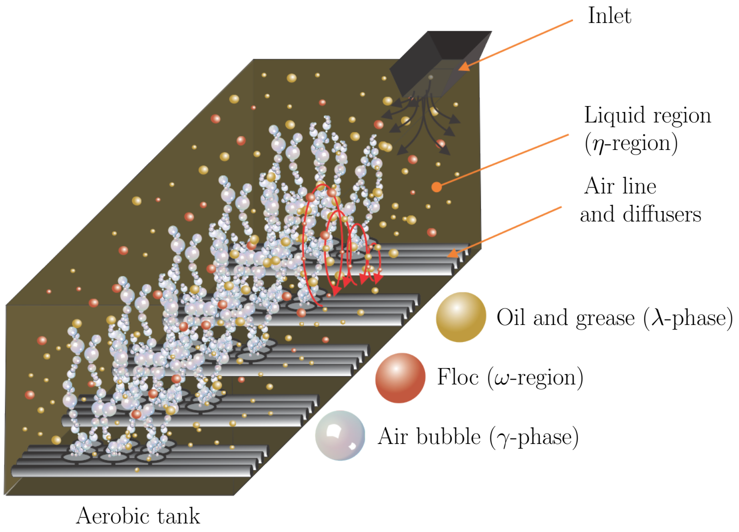

Fig. 1: Diagram of an aerobic tank in operation, identifying the phases and regions found in the system.

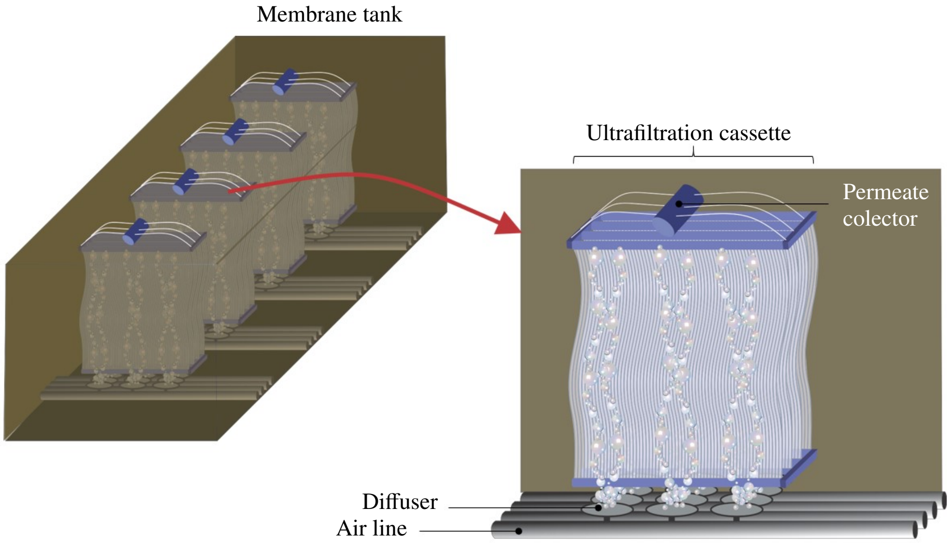

Fig. 2: Diagram of the membrane tank components: ultrafiltration cassette, permeate collector, diffusers and air lines.

The membrane tank is assumed not to contain flocs, therefore the consumption of both chemical species is minimal; hence, modeling transport of species-*B* is not considered in this tank. Consequently, the efficiency of the MBR relies only on the amount of species-*A* retained by the membrane. It should be added that, both tanks in the MBR constitute a multiphase and multiscale system. In the following paragraphs the mathematical models for each tank are derived.

3 Aerobic tank model

3.1 Microscale transport description

The derivation of the macroscopic models for both species (LCFA and oxygen) commences with the statement of the governing equations at the microscale. To this end, it is convenient to adopt the following set of starting assumptions:

1. The biofilm formation at the tank walls is negligible with respect to the amount of biomass in the flocs.
2. The concentration of non-flocculated microorganisms is negligible with respect to the concentration of microorganisms in the flocs.
3. Inert solids do not transport between phases or react.
4. pH and temperature remain constant.
5. There are resistances to mass transport between the γ-phase and the η-region. The same is true at the boundary between the λ-phase and the η-region.
6. The chemical reaction of hydrolysis follows first-order kinetics and takes place at the boundary between the λ-phase and the η-region.
7. There is no mass transport directly between the gas or oil phases and the flocs.
8. Momentum transport is quasi-steady with respect to mass transport.

On the basis of the above set of assumptions, the total mass continuity equations in both the η-region and the γ-phase can be expressed as follows:

$$\frac{\partial \rho_j}{\partial t} + \nabla \cdot (\rho_j \mathbf{v}_j) = 0, \quad j = \eta, \gamma \tag{1}$$

where ρ_j and $\mathbf{v}_j$ represent the j-zone density and velocity, respectively.

At this point, it is worth mentioning that the interest in this tank is to derive a model that describes the concentration dynamics and not necessarily the spatial variations of the concentration (except inside the flocs). Therefore, the assumption that momentum transport is quasi-steady makes it unnecessary to consider the momentum-transport equations in this tank. In this way, the attention can now be directed towards the species conservation equations in the different phases and regions within the tank. The governing equations in the η-region and in the γ-phase correspond to the classical species transport equations under passive conditions for both chemical species ($i = A, B$):

$$\frac{\partial c_{i\eta}}{\partial t} + \nabla \cdot (c_{i\eta}\mathbf{v}_{i\eta}) = 0, \quad \text{in the } \eta\text{-region} \tag{2a}$$

$$\frac{\partial c_{B\gamma}}{\partial t} + \nabla \cdot (c_{B\gamma}\mathbf{v}_{B\gamma}) = 0, \quad \text{in the } \gamma\text{-phase} \tag{2b}$$

The mathematical model to describe mass transport inside the flocs is not derived here because it is already available from de los Santos-Sánchez, Valdés-Parada, and Chirino (2016) and it can be written as ($i = A, B$):

$$\left(\varepsilon_{P_{ij}} K_{ij}^{-1} + \varepsilon_{ej}\right) \frac{\partial c_{i\omega j}}{\partial t} = D_{ij} \nabla^2 c_{i\omega j} - \varepsilon_{P_A j} \mu_{ij} \frac{c_{i\omega j}}{c_{i\omega j} + \alpha_{P_i}}, \quad \text{in the } \omega j\text{-region} \tag{2c}$$

In equations (2), c and $\mathbf{v}$ denote the molar concentration and the chemical species velocity in the fluid, respectively. In both cases, the first subscript identifies the chemical species and the second one identifies the zone. In addition, K_{ij}^{-1} is defined as the thermodynamic equilibrium constant that relates the concentration of species i between the extracellular matrix and the P_i-region. Moreover, ε_{ej} and $\varepsilon_{P_{ij}}$ are the volumetric fractions of the extracellular and the ωj regions that correspond to species i consuming cells, respectively. Also, μ_{ij} is the maximum specific consumption rate and α_{P_i} the half-saturation constant of species i consuming cells in the ωj region.

The effective-medium equation in the ω-region shows that, at the floc-scale, mass is only transported by effective diffusion. In addition, equation (2c) incorporates a homogeneous reaction term that results from the upscaling process at the cellular scale level (de los Santos-Sánchez et al., 2016). Indeed, the use of this model requires accepting an additional set of assumptions such as the local equilibrium hypothesis and the existence of a separation of length scales between the flocs and the distance between cells. This model considers two cellular types: cells that consume species i ($i = A, B$) (*i.e.*, the P_i-region) and cells that, for various reasons, do not consume the substrate (the N_i-region). Moreover, assuming that there is no substrate inhibition mechanism, the proposed reaction kinetics is of the Michaelis-Menten type. In fact, in the literature there are reports of the application of such a model to describe the oxidation of different types of fats (Becker, Abu-Reesh, Markossian, Antranikian, & Märkl, 1997; Hsu, Hanaki, & Matsumoto, 1983; Nakhla et al., 2006). Furthermore, floc size distributions are considered here and for this reason the subscript j is used in equation (2c), which runs from 1 to Nf, the latter denoting the number of floc sizes. Regarding the diffusive term, it is important to mention that the effective diffusion coefficient of species i (D_{ij}) was assumed to be isotropic at the cellular scale. As shown by de los Santos-Sánchez et al. (2016), this coefficient can be predicted from the solution of the associated closure problem and can be represented using analytical expressions as discussed later on.

The above differential equations are subject to the following set of boundary conditions that describe the mass transport phenomena taking place between the regions and phases ($i = A, B$):

$$\mathbf{n}_{\eta\lambda} \cdot c_{j\eta}(\mathbf{v}_{j\eta} - \mathbf{w}_{\eta\lambda k}) = -\delta_{jA} k_{\lambda\eta} c_\lambda, \quad \text{at } \mathscr{A}_{\eta\lambda k} \tag{3a}$$

$$\mathbf{n}_{\eta\omega} \cdot c_{i\eta}(\mathbf{v}_{i\eta} - \mathbf{w}_{\eta\omega j}) = \mathbf{n}_{\eta\omega} \cdot c_{i\omega j}(\mathbf{v}_{i\omega j} - \mathbf{w}_{\eta\omega j}), \text{at } \mathscr{A}_{\eta\omega j} \tag{3b}$$

$$\mathbf{n}_{\eta\omega} \cdot c_{i\eta}(\mathbf{v}_{i\eta} - \mathbf{w}_{\eta\omega j}) = k_{ij}^{\eta\omega}(c_{i\eta} - c_{i\omega j}), \quad \text{at } \mathscr{A}_{\eta\omega j} \tag{3c}$$

$$\mathbf{n}_{\gamma\eta} \cdot c_{B\gamma}(\mathbf{v}_{B\gamma} - \mathbf{w}_{\gamma\eta}) = \mathbf{n}_{\gamma\eta} \cdot c_{B\eta}(\mathbf{v}_{B\eta} - \mathbf{w}_{\gamma\eta}), \text{at } \mathscr{A}_{\gamma\eta} \tag{3d}$$

$$\mathbf{n}_{\gamma\eta} \cdot c_{B\gamma}(\mathbf{v}_{B\gamma} - \mathbf{w}_{\gamma\eta}) = k^{\gamma\eta}(c_{B\gamma} - c_{B\eta}), \quad \text{at } \mathscr{A}_{\gamma\eta} \tag{3e}$$

$$\mathbf{n}_{\gamma\omega} \cdot c_{B\gamma}(\mathbf{v}_{B\gamma} - \mathbf{w}_{\gamma\omega j}) = 0, \quad \text{at } \mathscr{A}_{\gamma\omega j} \tag{3f}$$

$$\mathbf{n}_{\gamma i} \cdot c_{ik}(\mathbf{v}_{ik} - \mathbf{w}_{\gamma j}) = 0, \quad j = \eta, \lambda, k = \eta, \gamma, \text{at } \mathscr{A}_{\gamma j} \tag{3g}$$

In these equations, $\mathbf{n}$ is the unit normal vector, directed from the first to the second zone indicated at its subscripts, and $\mathbf{w}$ is the speed of displacement of the boundary between the two zones. Additionally, δ_{jA} is the Kronecker delta, $k_{\lambda\eta}$ is the hydrolysis reaction constant at the $\lambda\eta$ boundary, $k_{ij}^{\eta\omega}$ is the interfacial mass transport coefficient between the zones indicates at its superscripts for species i in the j floc size, and $k^{\gamma\eta}$ is the interfacial oxygen mass transport coefficient at the $\gamma\eta$ boundary. Finally, $\mathscr{A}_{kl}$ represents the boundary between the k and l zones.

At $\mathscr{A}_{\eta\lambda}$ there is a generation reaction of species A, due to the hydrolysis of the oils and greases under the form of a first-order reaction in equation (3a). Here, the subscript k identifies the size distribution of oil micelles. Moving on to the $\mathscr{A}_{\eta\omega}$ surface, it is assumed that surface accumulation, reaction and deformation are negligible with respect to normal mass flux and that there are interfacial mass transport resistances that can be modeled by means of Newton's cooling law for both species, as shown in equations (3b) and (3c). Similar assumptions are imposed at $\mathscr{A}_{\gamma\eta}$, as reported in equations (3d) and (3e). Furthermore, as expressed in equation (3f), there is no transport of species B from the γ-phase into the ω-region. Finally, no transport of species A and B takes place in the rest of the boundaries as reported in equations (3f) and (3g).

Since the λ-phase contains oils and greases with different chemical structures from those transported in the η and ω regions, it is not necessary to consider them in the model. Certainly, the statement of the microscale model requires imposition of the boundary conditions at the macroscopic inlets and outlets as well as the corresponding initial conditions. However, this information is not required for the derivation of the upscaled model and it is not reported at this point for the sake of brevity in presentation.

3.2 Upscaling

This section is dedicated to the derivation of the upscaled models for mass transport in the η-region (for both chemical species) and in the γ-phase (for species B). Since the model for the ω-region is already an effective-medium equation, it does not require further upscaling. To this end, let $\mathscr{V}_j$ (of volume V_j) denote the space occupied by the j-zone within the aerobic tank, where $j = \eta, \gamma$. In terms of this domain, it is convenient to introduce the following intrinsic averaging operator for any piece-wise smooth quantity, ψ:

$$\psi^j = \frac{1}{V_j} \int_{\mathscr{V}_j} \psi_j \, dV \tag{4}$$

Application of this averaging operator to the continuity equations (1), assuming incompressible flow and taking into account the transient dependence of V_j leads, after the use of the general transport theorem and the divergence theorem (Bird, Stewart, & Lightfoot, 2002), to the following expressions:

$$\frac{dV_\eta}{dt} = \dot{Q}_{i\eta} - \dot{Q}_{o\eta} \tag{5a}$$

$$\frac{dV_\gamma}{dt} = \dot{Q}_{d\gamma} - \dot{Q}_{sup\gamma} \tag{5b}$$

In the above equations $\dot{Q}$ denotes the volumetric flow rate at specific boundaries identified by the subscripts. In the η-region, the inlet corresponds to the inflow of the tank (identified by the subscript $i\eta$) and the outlet stream is identified by $o\eta$. For the γ-phase, the inlet ($d\gamma$) corresponds to the diffusers and the outlet ($sup\gamma$) corresponds to the upper surface of the liquid in the tank.

For species A and B, a similar procedure can be applied to equations (2a) and (2b), taking into account the corresponding boundary conditions to obtain the following set of upscaled equations:

$$\frac{dc_A^\eta}{dt} = \frac{\dot{Q}_{e\eta}}{V_\eta}(c_{A\eta e} - c_A^\eta) - \sum_{j=1}^{j=Nf} \frac{k_{Aj}^{\eta\omega} A_{\eta\omega j}}{V_\eta}(c_A^\eta - c_{A\omega j}) + \frac{k_{\lambda\eta} c_\lambda A_{\eta\lambda}}{V_\eta}, \quad \text{in the } \eta\text{-region} \tag{6a}$$

$$\frac{dc_B^\gamma}{dt} = \frac{\dot{Q}_{d\gamma}}{V_\gamma}(c_{B\gamma d} - c_B^\gamma) - \frac{k^{\gamma\eta} A_{\eta\gamma}}{V_\gamma}(c_B^\gamma - c_B^\eta), \quad \text{in the } \gamma\text{-phase} \tag{6b}$$

$$\frac{dc_B^\eta}{dt} = -\frac{\dot{Q}_{e\eta}}{V_\eta} c_B^\eta - \sum_{j=1}^{j=Nf} \frac{k_{Bj}^{\eta\omega} A_{\eta\omega j}}{V_\eta}(c_B^\eta - c_{B\omega j}) - \frac{k^{\gamma\eta} A_{\eta\gamma}}{V_\eta}(c_B^\eta - c_B^\gamma), \quad \text{in the } \eta\text{-region} \tag{6c}$$

Here, c_i^k denotes the average concentration of species i in the k-zone. Also, $c_{A\eta e}$ indicates the species A concentration at the inlet, $c_{B\gamma d}$ the species B concentration in the γ-phase inlet (diffusers), and A_{kl} the interfacial area between the k and l zones.

At this point, it is worth mentioning that the derivation of these equations requires assuming that the concentrations of the species at the interfaces can be approximated by its intrinsic averages. This assumption is reasonable as long as well-mixed conditions are applicable in the system. Clearly, the above equations are coupled with the concentrations resulting from the solutions of equation (2c), which, for the sake of simplicity, is assumed from this point on to be applicable in spherical coordinates. This assumption should be regarded as a modeling choice and if it is not realistic, it can be easily relaxed. In addition, to facilitate the mathematical treatment, mass transport is assumed to be symmetric in all directions within each sphere. Under these conditions, the upscaled model only requires to specify the following set of initial conditions to complete its statement ($i = A, B$):

$$\text{When } t = 0, \quad c_B^\gamma = c_{B0}^\gamma, \quad c_i^\eta = c_{i0}^\eta, \quad c_{i\omega j} = c_{i\omega j0} \tag{7}$$

with all the terms on the right-hand side of the above equations being known quantities.

4 Membrane tank model

In this section the attention is drawn upon mass and momentum transport within the ultrafiltration cassettes (*i.e.*, the ζ-region). The goal is to derive effective medium models for both types of transport phenomena using the volume averaging method under a mechanical equilibrium approximation. The transport equations for the η-region outside the cassettes correspond to their microscale counterparts inside the cassettes and they do not require to be upscaled.

4.1 Microscale transport description

Similarly to the aerobic tank, the following set of starting assumptions are adopted in order to develop the membrane tank models:

1. Incompressible and Newtonian flow.
2. Quasi-stationary state for momentum transport.
3. The concentration of species A is sufficiently diluted in order to apply Fick's law.
4. The hollow fibre matrix is inert.
5. Air bubbles have spherical geometry and no size distribution is considered.
6. The concentration of microorganisms in this tank is negligible with respect to the concentration in the aerobic tank. Therefore, oils and greases oxidation is not considered.
7. The concentration and hydrolysis of oils and greases in the membrane tank is negligible compared to the concentration and hydrolysis in the aerobic tank.
8. Solids are mechanically inert, hence, they do not transport or react and are rejected by the membrane.
9. pH and temperature are constant.
10. There are resistances to mass transport between the η-region (or the β-phase) and the σ-region.

On the basis of these constraints, the governing equations at the microscale for mass and momentum transport are the following ($k = \gamma, \eta, \sigma$; $j = \gamma, \eta$):

$$\nabla \cdot \mathbf{v}_k = 0, \quad \text{in the } k\text{-zone} \tag{8a}$$

$$\rho_j \mathbf{v}_j \cdot \boldsymbol{\nabla} \mathbf{v}_j = -\boldsymbol{\nabla} \widetilde{\mathscr{P}_j} + \mu_j \nabla^2 \mathbf{v}_j - \boldsymbol{\nabla} \langle \mathscr{P}_j \rangle^j, \quad \text{in the } j\text{-zone} \tag{8b}$$

$$\mathbf{v}_\sigma = -\frac{\mathsf{H}_\sigma}{\mu} \cdot \boldsymbol{\nabla} \mathscr{P}^\sigma, \quad \text{in the } \sigma\text{-region} \tag{8c}$$

In the previous set of equations, $\mathbf{v}_k$, $\mathbf{v}_j$ and $\mathbf{v}_\sigma$ stand for the fluid velocity in the corresponding zone at its subscript. In equation (8b), the spatial decomposition proposed by Gray (1975) was used for the dynamic pressure in each region: $\mathscr{P}_j = \langle \mathscr{P}_j \rangle^j + \widetilde{\mathscr{P}_j}$; with this decomposition, the pointwise pressure is divided in its intrinsic average and its spatial deviations in the j-zone. The intrinsic averaging operator in the ζ-region is defined as follows:

$$\langle \psi \rangle^j = \frac{1}{V_j} \int_{\mathscr{V}_j} \psi \, dV \tag{8d}$$

Here V_j is the volume occupied by the j-zone within a representative averaging domain suitable for the ζ-region. In addition, equation (8c) corresponds to the effective-medium model for momentum transport derived by Whitaker (1996). In this equation, H_σ corresponds to an apparent permeability tensor for the σ-region. The values of the components of this tensor can be predicted from the solution of the associated closure problem as reported by Lasseux, Arani, and Ahmadi (2011). Moreover, μ is the viscosity of the region and $\mathscr{P}^\sigma$ is the intrinsic average of the dynamic pressure in the σ-region.

At the boundaries of the η-region and the β-phase in contact with the porous medium (*i.e.*, the σ-phase), it is assumed that the normal component of the velocity is continuous ($j = \eta, \beta$):

$$\mathbf{n}_{j\sigma} \cdot \mathbf{v}_j = \mathbf{n}_{j\sigma} \cdot \mathbf{v}_\sigma, \quad \text{at } \mathscr{A}_{j\sigma} \tag{8e}$$

In addition, a jump for its tangential component is assumed, which is described by the vectorial form of the Beavers and Joseph (1967) boundary condition for inertial flow:

$$(\mathsf{I} - \mathbf{n}_{j\sigma}\mathbf{n}_{j\sigma}) \cdot \left[\mathbf{n}_{j\sigma} \cdot \left(\rho_j \mathbf{v}_j \mathbf{v}_j - \mu \left[\boldsymbol{\nabla} \mathbf{v}_j + (\boldsymbol{\nabla} \mathbf{v}_j)^T\right]\right)\right] = \frac{\alpha_\sigma}{\sqrt{\|\mathsf{H}_\sigma\|}} \left(\mathbf{v}_j + \frac{\mathsf{H}_\sigma}{\mu} \cdot \boldsymbol{\nabla} \langle \mathscr{P}^\sigma \rangle^\sigma + \frac{\mathsf{H}_\sigma}{\mu} \cdot \boldsymbol{\nabla} \widetilde{\mathscr{P}^\sigma}\right), \quad \text{at } \mathscr{A}_{j\sigma} \tag{8f}$$

where α_σ is a jump coefficient that takes into account the transition from flow in a free-fluid zone and into a porous medium. The values of this coefficient may certainly be altered by fouling of the fibers in the ultrafiltration cassettes. At the boundary between the γ-phase and the σ-region, the no-slip boundary condition is imposed:

$$\mathbf{v}_\gamma = \mathbf{0}, \quad \text{at } \mathscr{A}_{\gamma\sigma} \tag{8g}$$

Directing the attention to the boundary between the η-region and the γ-phase, it is reasonable to assume mechanical equilibrium of the velocities. Therefore, the following continuity condition may be imposed:

$$\mathbf{v}_\gamma = \mathbf{v}_\eta, \quad \text{at } \mathscr{A}_{\gamma\eta} \tag{8h}$$

Furthermore, the boundary condition corresponding to momentum transport implies the use of the Young-Laplace equation as well as the following assumption:

$$\begin{aligned}&(\rho_\eta - \rho_\gamma) g y_{\eta\gamma} \ll \max\left(\widetilde{\mathscr{P}}_\eta, \widetilde{\mathscr{P}}_\gamma\right),\\ &\max\left(\mu\left[\nabla \mathbf{v}_\eta + (\nabla \mathbf{v}_\eta)^T\right], \mu_\gamma\left[\nabla \mathbf{v}_\gamma + (\nabla \mathbf{v}_\gamma)^T\right]\right)\end{aligned} \tag{8i}$$

so that the following boundary condition results:

$$\begin{aligned}&\mathbf{n}_{\eta\gamma} \cdot \left(\widetilde{\mathscr{P}}_\eta \mathbf{I} - \mu\left[\nabla \mathbf{v}_\eta + (\nabla \mathbf{v}_\eta)^T\right]\right)\\ &= \mathbf{n}_{\eta\gamma} \cdot \left(\widetilde{\mathscr{P}}_\gamma \mathbf{I} - \mu_\gamma\left[\nabla \mathbf{v}_\gamma + (\nabla \mathbf{v}_\gamma)^T\right]\right), \quad \text{at } \mathscr{A}_{\eta\gamma}\end{aligned} \tag{8j}$$

In equation (8i), $g y_{\eta\gamma}$ represents the order of magnitude estimate of the inner product between the gravity and a vector locating points at the interface relative to the centroid of the averaging domain.

To complete the problem statement, it is worth noting that the above equations are to be formally solved in a periodic unit cell that is representative of the ζ-region, such as the one sketched in figure 3. At this point, it is pertinent to remark that the use of a unit cell model to carry out the analysis is reasonable as long as there is a separation of length scales. For the case at hand, it is required for the characteristic length of the ultrafiltration cassettes to be much larger than the one corresponding to microscale transport within the phases and regions of the system. For this solution domain, it is reasonable to impose the following periodic boundary conditions ($j = \eta, \gamma$, $k = \beta, \sigma$):

$$\psi_j(\mathbf{r}_j + \mathbf{l}_i) = \psi_j(\mathbf{r}_j), \quad i = 1,2,3; \quad \psi = \mathbf{v}, \widetilde{\mathscr{P}} \tag{8k}$$

$$\psi_k(\mathbf{r}_k + \mathbf{l}_3) = \psi_k(\mathbf{r}_k); \quad \psi = \mathbf{v}, \widetilde{\mathscr{P}} \tag{8l}$$

where $\mathbf{r}_j$ and $\mathbf{r}_k$ are position vectors, and $\mathbf{l}_i$ and $\mathbf{l}_3$ are the unit cell lattice vectors in the i or third direction, respectively.

Finally, the fields of the deviations of the dynamic pressure are bounded by the following average constraint, which is a corollary of the separation of length scales mentioned above ($j = \eta, \gamma, \beta, \sigma$):

$$\left\langle \widetilde{\mathscr{P}}_j \right\rangle^j = 0 \tag{8m}$$

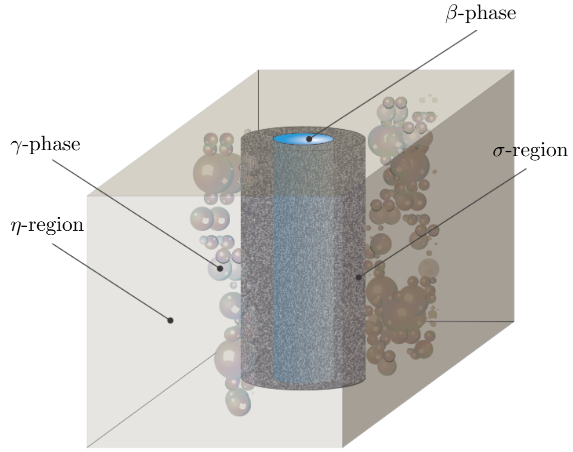

Fig. 3: Sketch of a representative periodic unit cell for the ultrafiltration cassette of the membrane tank, identifying the phases and regions involved.

Equations (8) are sufficient to carry out the upscaling process for momentum transport as shown below. For now, it is pertinent to present the governing equations for mass transport of species A. To this end, it is worth noting that no chemical reaction takes place in the system. For this reason, the governing equation in the σ-region corresponds to the one derived by Whitaker (1999):

$$\frac{\partial c_{A\sigma}}{\partial t} + \nabla \cdot (c_{A\sigma} \mathbf{v}^\sigma) = \nabla \cdot (\mathbf{D}^* \cdot \nabla c_{A\sigma}), \text{in the } \sigma\text{-region} \tag{9a}$$

whereas the equations for the other regions of the system are simply the convection-diffusion equations ($j = \eta, \beta$):

$$\frac{\partial c_{Aj}}{\partial t} + \nabla \cdot (c_{Aj} \mathbf{v}_j) = \nabla \cdot (\mathscr{D}_{Aj} \nabla c_{Aj}), \text{in the } j\text{-zone} \tag{9b}$$

In equation (9a), $\mathbf{v}^\sigma$ denotes the intrinsic average of the velocity of the β-phase inside the σ-region. While $\mathbf{D}^*$ represents the total dispersion tensor, which can be calculated from the solution of the associated closure problem derived by Whitaker (1999), and $\mathscr{D}_{Aj}$ is the molecular diffusivity of species A in the j-zone.

At the boundary between the η-region (or the β-phase) and the σ-region, the contributions of accumulation and surface transport are neglected with respect to perpendicular mass transport. Furthermore, it is considered that the hollow fibers do not experiment changes at their surface. Moreover, mass transport resistances are considered at this boundary.

Consequently, the corresponding boundary conditions at these surfaces are the following ($j = \eta,\beta$):

$$\mathbf{n}_{j\sigma} \cdot c_{A\eta}\mathbf{v}_{Aj} = \mathbf{n}_{j\sigma} \cdot c_{A\sigma}\mathbf{v}_{A\sigma}, \quad \text{at } \mathscr{A}_{j\sigma} \tag{10a}$$

$$\mathbf{n}_{j\sigma} \cdot c_{Aj}\mathbf{v}_{Aj} = k^{\sigma j}(c_{Aj} - c_{A\sigma}), \quad \text{at } \mathscr{A}_{j\sigma} \tag{10b}$$

In the previous equations, $k_{\sigma j}$ represents the interfacial mass transport coefficient, given for the species A at the boundary between the j and the σ zones. Certainly, this coefficient accounts for fouling taking place in the fibers of the ultrafiltration cassettes. Finally, there is no mass transport of species A between the γ-phase and the σ-region:

$$\mathbf{n}_{\gamma\sigma} \cdot c_{A\gamma}\mathbf{v}_{A\gamma} = 0, \quad \text{at } \mathscr{A}_{\gamma\sigma} \tag{10c}$$

4.2 *Upscaling*

The derivation of the upscaled transport models is presented in the following manner: First, the corresponding model for total mass transport is derived, second the macroscopic momentum transport model is addressed. Finally, the attention is directed towards the derivation of an effective-medium equation for mass transport of species-A. This last model is derived under the local equilibrium assumption. The term *local equilibrium* refers, unlike *thermodynamic equilibrium*, to the equality of average quantities, between the different phases or regions, but it does not imply the absence of spatio-temporal changes (Whitaker, 1999).

To commence the upscaling process, it is necessary to define an averaging domain, $\mathscr{V}$ containing portions of all the phases and regions involved in the cassette. In this way, the following superficial averaging operator can be defined ($j = \gamma, \eta, \sigma, \beta$):

$$\langle \psi_j \rangle_j = \frac{1}{V}\int_{\mathscr{V}_j} \psi_j \, dV \tag{11}$$

In order to derive the macroscopic model for total mass conservation in the η-region, the process consists of: averaging the equation (8a) and applying the spatial averaging theorem (Howes & Whitaker, 1985), taking into account the corresponding boundary conditions, leading to:

$$\nabla \cdot \langle \mathbf{v}_\eta \rangle_\eta + \frac{1}{V}\int_{\mathscr{A}_{\eta\gamma}} \mathbf{n}_{\eta\gamma} \cdot \mathbf{v}_\gamma \, dA + \frac{1}{V}\int_{\mathscr{A}_{\eta\sigma}} \mathbf{n}_{\eta\sigma} \cdot \mathbf{v}_\sigma \, dA = 0 \tag{12a}$$

Using a similar approach, it renders the following macroscale continuity equations for the remaining phases and regions:

$$\nabla \cdot \langle \mathbf{v}_\gamma \rangle_\gamma + \frac{1}{V}\int_{\mathscr{A}_{\gamma\eta}} \mathbf{n}_{\gamma\eta} \cdot \mathbf{v}_\gamma \, dA = 0 \tag{12b}$$

$$\nabla \cdot \langle \mathbf{v}_\beta \rangle_\beta + \frac{1}{V}\int_{\mathscr{A}_{\beta\sigma}} \mathbf{n}_{\beta\sigma} \cdot \mathbf{v}_\sigma \, dA = 0 \tag{12c}$$

$$\nabla \cdot \langle \mathbf{v}_\sigma \rangle_\sigma + \frac{1}{V}\int_{\mathscr{A}_{\sigma\eta}} \mathbf{n}_{\sigma\eta} \cdot \mathbf{v}_\sigma \, dA + \frac{1}{V}\int_{\mathscr{A}_{\sigma\beta}} \mathbf{n}_{\sigma\beta} \cdot \mathbf{v}_\sigma \, dA = 0 \tag{12d}$$

Adding all the above average equations, it gives rise to the following macroscopic mass equation:

$$\nabla \cdot \langle \mathbf{v} \rangle = 0 \tag{13}$$

Here, the following definition was used:

$$\langle \mathbf{v} \rangle = \frac{1}{V}\int_{\mathscr{V}} \mathbf{v} \, dV \tag{14}$$

In order to derive the macroscopic equation for momentum transport, it is pertinent to direct the attention to the microscale model given in equations (8). In this problem, four source terms can be identified, namely: $\nabla\langle \mathscr{P}_\eta \rangle^\eta$, $\nabla\langle \mathscr{P}_\gamma \rangle^\gamma$, $\nabla\langle \mathscr{P}_\beta \rangle^\beta$ and $\nabla\langle \mathscr{P}_\sigma \rangle^\sigma$. Consequently, the following formal solutions can be proposed for the velocity and the dynamic pressure deviations ($j = \eta, \gamma, \beta, \sigma$):

$$\begin{aligned} \mathbf{v}_j = &-\frac{\mathsf{D}_{j\eta}}{\mu} \cdot \nabla\langle \mathscr{P}_\eta \rangle^\eta - \frac{\mathsf{D}_{j\gamma}}{\mu_\gamma} \cdot \nabla\langle \mathscr{P}_\gamma \rangle^\gamma \\ &- \frac{\mathsf{D}_{j\beta}}{\mu} \cdot \nabla\langle \mathscr{P}_\beta \rangle^\beta - \frac{\mathsf{D}_{j\sigma}}{\mu} \cdot \nabla\langle \mathscr{P}_\sigma \rangle^\sigma \end{aligned} \tag{15a}$$

$$\begin{aligned} \widetilde{\mathscr{P}}_j = &-\frac{\mathbf{d}_{j\eta}}{\mu} \cdot \nabla\langle \mathscr{P}_\eta \rangle^\eta - \frac{\mathbf{d}_{j\gamma}}{\mu_\gamma} \cdot \nabla\langle \mathscr{P}_\gamma \rangle^\gamma \\ &- \frac{\mathbf{d}_{j\beta}}{\mu} \cdot \nabla\langle \mathscr{P}_\beta \rangle^\beta - \frac{\mathbf{d}_{j\sigma}}{\mu} \cdot \nabla\langle \mathscr{P}_\sigma \rangle^\sigma \end{aligned} \tag{15b}$$

where the closure variables D_{ij} and $\mathbf{d}_{ij}$ map the influence of each source onto $\mathbf{v}_j$ and $\widetilde{\mathscr{P}}_j$, respectively. The governing equations for the closure variables are not reported in this document for the sake of brevity in presentation. On the basis of the above solution, the corresponding macroscale model results from applying the superficial averaging operator to equation (15a) and it can be written as follows ($j =$

η,γ,β,σ):

$$\langle \mathbf{v}_j \rangle_j = -\frac{\mathsf{H}_{j\eta}}{\mu} \cdot \nabla \langle \mathscr{P}_\eta \rangle^\eta - \frac{\mathsf{H}_{j\gamma}}{\mu_\gamma} \cdot \nabla \langle \mathscr{P}_\gamma \rangle^\gamma - \frac{\mathsf{H}_{j\beta}}{\mu} \cdot \nabla \langle \mathscr{P}_\beta \rangle^\beta - \frac{\mathsf{H}_{j\sigma}}{\mu} \cdot \nabla \langle \mathscr{P}_\sigma \rangle^\sigma \tag{16}$$

In the previous equation, the apparent permeability tensors are defined as: $\mathsf{H}_{j\eta} = \langle \mathsf{D}_{j\eta} \rangle_\eta$, $\mathsf{H}_{j\gamma} = \langle \mathsf{D}_{j\gamma} \rangle_\eta$, $\mathsf{H}_{j\beta} = \langle \mathsf{D}_{j\beta} \rangle_\eta$, $\mathsf{H}_{j\sigma} = \langle \mathsf{D}_{j\sigma} \rangle_\eta$. The above equation can be significantly simplified using the mechanical equilibrium assumption, which allows equating all the macroscopic pressure gradients as a single one. In this way, the following Darcy-like model results:

$$\langle \mathbf{v} \rangle = -\frac{\mathsf{H}}{\mu_{av}} \cdot \nabla \langle \mathscr{P} \rangle \tag{17}$$

Here, the ratio of the total apparent permeability tensor and the average viscosity is defined as ($j = \eta,\gamma,\beta,\sigma$):

$$\frac{\mathsf{H}}{\mu_{av}} = \frac{\mathsf{H}_{j\eta}}{\mu} + \frac{\mathsf{H}_{j\gamma}}{\mu_\gamma} + \frac{\mathsf{H}_{j\beta}}{\mu} + \frac{\mathsf{H}_{j\sigma}}{\mu} \tag{18}$$

Hence, the closed form of the macroscopic models for total mass and momentum transport are given by equations (13) and (17), respectively, and the attention can be directed to the upscaling of species-A mass transport. Application of the intrinsic averaging operator (equation 8d) to equation (9a), followed by the use of the spatial averaging theorem and the corresponding boundary conditions, lead to:

$$\frac{\partial \langle c_{A\sigma} \rangle^\sigma}{\partial t} + \nabla \cdot \langle c_{A\sigma} \mathbf{v}^\sigma \rangle^\sigma - \frac{k^{\sigma\eta}}{V_\sigma} \int_{\mathscr{A}_{\sigma\eta}} (c_{A\eta} - c_{A\sigma})\, dA + \frac{k^{\sigma\beta}}{V_\sigma} \int_{\mathscr{A}_{\sigma\beta}} (c_{A\sigma} - c_{A\beta})\, dA = \nabla \cdot \left[\mathsf{D}^* \cdot \left(\nabla \langle c_{A\sigma} \rangle^\sigma + \frac{1}{V_\sigma} \int_{\mathscr{A}_\sigma} \mathbf{n}_\sigma c_{A\sigma}\, dA \right) \right] \tag{19}$$

This result can be further worked after introducing the spatial decomposition for the concentration in the corresponding integral filters, giving rise to:

$$\frac{\partial \langle c_{A\sigma} \rangle^\sigma}{\partial t} + \nabla \cdot (\langle c_{A\sigma} \rangle^\sigma \langle \mathbf{v}^\sigma \rangle^\sigma) + \nabla \cdot \langle \tilde{c}_{A\sigma} \mathbf{v}^\sigma \rangle^\sigma - \frac{k^{\sigma\eta} a_{\sigma\eta}}{\varepsilon_\sigma} (\langle c_{A\eta} \rangle^\eta - \langle c_{A\sigma} \rangle^\sigma) - \frac{k^{\sigma\eta} a_{\sigma\eta}}{\varepsilon_\sigma A_{\sigma\eta}} \int_{\mathscr{A}_{\sigma\eta}} (\tilde{c}_{A\eta} - \tilde{c}_{A\sigma})\, dA + \frac{k^{\sigma\beta} a_{\sigma\beta}}{\varepsilon_\sigma} (\langle c_{A\sigma} \rangle^\sigma - \langle c_{A\beta} \rangle^\beta) + \frac{k^{\sigma\beta} a_{\sigma\beta}}{\varepsilon_\sigma A_{\sigma\beta}} \int_{\mathscr{A}_{\sigma\beta}} (\tilde{c}_{A\sigma} - \tilde{c}_{A\beta})\, dA = \nabla \cdot \left[\mathsf{D}^* \cdot \left(\nabla \langle c_{A\sigma} \rangle^\sigma + \frac{1}{V_\sigma} \int_{\mathscr{A}_\sigma} \mathbf{n}_{\sigma\beta} \tilde{c}_{A\sigma}\, dA \right) \right] \tag{20a}$$

Here, $a_{\sigma\eta}$ and $a_{\sigma\beta}$ stand for the interfacial areas per unit volume for the boundaries between the σ and the j-zones, and ε_j represents the volumetric fraction of the j-region. In the following, this model is referred to as the *unclosed average model* for the σ-region because it is expressed in terms of deviation quantities, which are unknown at this point of the derivations. Performing a similar analysis to the remaining regions and phases of the system, the following unclosed average models result:

$$\frac{\partial \langle c_{A\eta} \rangle^\eta}{\partial t} + \nabla \cdot \left(\langle c_{A\eta} \rangle^\eta \langle \mathbf{v}_\eta \rangle^\eta \right) + \nabla \cdot \langle \tilde{c}_{A\eta} \mathbf{v}_\eta \rangle^\eta + \frac{k^{\sigma\eta} a_{\sigma\eta}}{\varepsilon_\eta} (\langle c_{A\eta} \rangle^\eta - \langle c_{A\sigma} \rangle^\sigma) + \frac{k^{\sigma\eta} a_{\sigma\eta}}{\varepsilon_\eta A_{\eta\sigma}} \int_{\mathscr{A}_{\eta\sigma}} (\tilde{c}_{A\eta} - \tilde{c}_{A\sigma})\, dA = \nabla \cdot \left[\mathscr{D}_{A\eta} \left(\nabla \langle c_{A\eta} \rangle^\eta + \frac{1}{V_\eta} \int_{\mathscr{A}_\eta} \mathbf{n}_\eta \tilde{c}_{A\eta}\, dA \right) \right] \tag{20b}$$

$$\frac{\partial \langle c_{A\beta} \rangle^\beta}{\partial t} + \nabla \cdot \left(\langle c_{A\beta} \rangle^\beta \langle \mathbf{v}_\beta \rangle^\beta \right) + \nabla \cdot \langle \tilde{c}_{A\beta} \mathbf{v}_\beta \rangle^\beta - \frac{k^{\sigma\beta} a_{\sigma\beta}}{\varepsilon_\beta} (\langle c_{A\sigma} \rangle^\sigma - \langle c_{A\beta} \rangle^\beta) - \frac{k^{\sigma\beta} a_{\sigma\beta}}{\varepsilon_\beta A_{\beta\sigma}} \int_{\mathscr{A}_{\beta\sigma}} (\tilde{c}_{A\sigma} - \tilde{c}_{A\beta})\, dA = \nabla \cdot \left[\mathscr{D}_{A\beta} \left(\nabla \langle c_{A\beta} \rangle^\beta + \frac{1}{V_\beta} \int_{\mathscr{A}_{\beta\sigma}} \mathbf{n}_{\beta\sigma} \tilde{c}_{A\beta}\, dA \right) \right] \tag{20c}$$

In order to determine the concentration deviations, it is necessary to derive, simplify and solve their governing equations. This process is known as *closure* and it is briefly presented below. The differential equations for the concentration deviations are the result of subtracting the unclosed equations (20) to their microscale counterparts (equations 9). On the basis of the length scale constraint $\max(\ell_j) \ll L$, (with

ℓ_j being the characteristic length of the j-region and L denoting the cassette characteristic length) and the following temporal constraints in terms of the Biot and Péclet numbers:

$$\mathbf{O}\left(\frac{\ell_\sigma^2}{\mathscr{D}_{A\beta}\left(1+Pe_\sigma+\frac{Bi_{\sigma\eta}(\tilde{c}_{A\eta}-\tilde{c}_{A\sigma})}{\tilde{c}_{A\sigma}}+\frac{Bi_{\sigma\beta}(\tilde{c}_{A\sigma}-\tilde{c}_{A\beta})}{\tilde{c}_{A\sigma}}\right)}\right)\ll t^* \tag{21a}$$

$$\mathbf{O}\left(\frac{\ell_\eta^2}{\mathscr{D}_{A\eta}\left(1+Pe_\eta+\frac{Bi_{\eta\sigma}(\tilde{c}_{A\eta}-\tilde{c}_{A\sigma})}{\tilde{c}_{A\eta}}\right)}\right)\ll t^* \tag{21b}$$

$$\mathbf{O}\left(\frac{\ell_\beta^2}{\mathscr{D}_{A\beta}\left(1+Pe_\beta+\frac{Bi_{\beta\sigma}(\tilde{c}_{A\sigma}-\tilde{c}_{A\beta})}{\tilde{c}_{A\beta}}\right)}\right)\ll t^* \tag{21c}$$

the governing equations for the concentration deviations can be written, under a local-mass equilibrium framework (see details in Whitaker, 1999), as follows:

$$\begin{aligned}&\tilde{\mathbf{v}}^\sigma\cdot\nabla\langle c_A\rangle+\mathbf{v}^\sigma\cdot\nabla\tilde{c}_{A\sigma}=\nabla\cdot(\mathbf{D}^*\cdot\nabla\tilde{c}_{A\sigma})\\&-\frac{k^{\sigma\eta}a_{\sigma\eta}}{\varepsilon_\sigma A_{\sigma\eta}}\int_{\mathscr{A}_{\sigma\eta}}(\tilde{c}_{A\eta}-\tilde{c}_{A\sigma})\,dA\\&+\frac{k^{\sigma\beta}a_{\sigma\beta}}{\varepsilon_\sigma A_{\sigma\beta}}\int_{\mathscr{A}_{\sigma\beta}}(\tilde{c}_{A\sigma}-\tilde{c}_{A\beta})\,dA,\quad\text{in the }\sigma\text{-region}\end{aligned} \tag{22a}$$

$$\begin{aligned}&\tilde{\mathbf{v}}_\eta\cdot\nabla\langle c_A\rangle+\mathbf{v}_\eta\cdot\nabla\tilde{c}_{A\eta}=\nabla\cdot\left(\mathscr{D}_{A\eta}\nabla\tilde{c}_{A\eta}\right)\\&+\frac{k^{\sigma\eta}a_{\sigma\eta}}{\varepsilon_\eta A_{\eta\sigma}}\int_{\mathscr{A}_{\eta\sigma}}(\tilde{c}_{A\eta}-\tilde{c}_{A\sigma})\,dA,\quad\text{in the }\eta\text{-region}\end{aligned} \tag{22b}$$

$$\begin{aligned}&\tilde{\mathbf{v}}_\beta\cdot\nabla\langle c_A\rangle+\mathbf{v}_\beta\cdot\nabla\tilde{c}_{A\beta}=\nabla\cdot\left(\mathscr{D}_{A\beta}\nabla\tilde{c}_{A\beta}\right)\\&-\frac{k^{\sigma\beta}a_{\sigma\beta}}{\varepsilon_\beta A_{\beta\sigma}}\int_{\mathscr{A}_{\beta\sigma}}(\tilde{c}_{A\sigma}-\tilde{c}_{A\beta})\,dA,\quad\text{in the }\beta\text{-phase}\end{aligned} \tag{22c}$$

The above equations are subject to the following boundary conditions, which result from substituting the spatial decomposition of the concentration into equations (10) ($j=\eta,\beta$):

$$\begin{aligned}&\mathbf{n}_{j\sigma}\cdot\langle c_A\rangle\mathbf{v}_j-\mathbf{n}_{j\sigma}\cdot\mathscr{D}_{Aj}\nabla\langle c_A\rangle+\mathbf{n}_{j\sigma}\cdot\tilde{c}_{Aj}\mathbf{v}_j\\&-\mathbf{n}_{j\sigma}\cdot\mathscr{D}_{Aj}\nabla\tilde{c}_{Aj}=\mathbf{n}_{j\sigma}\cdot\langle c_A\rangle\mathbf{v}^\sigma-\mathbf{n}_{j\sigma}\cdot\mathscr{D}_{A\sigma}\nabla\langle c_A\rangle\\&+\mathbf{n}_{j\sigma}\cdot\tilde{c}_{A\sigma}\mathbf{v}^\sigma-\mathbf{n}_{j\sigma}\cdot\mathscr{D}_{A\sigma}\nabla\tilde{c}_{A\sigma},\quad\text{at }\mathscr{A}_{j\sigma}\end{aligned} \tag{22d}$$

$$\begin{aligned}&\mathbf{n}_{j\sigma}\cdot\left(\langle c_A\rangle\mathbf{v}_j-\mathscr{D}_{Aj}\nabla\langle c_A\rangle+\tilde{c}_{Aj}\mathbf{v}_j-\mathscr{D}_{Aj}\nabla\tilde{c}_{Aj}\right)\\&=k^{\sigma j}(\tilde{c}_{Aj}-\tilde{c}_{A\sigma}),\quad\text{at }\mathscr{A}_{j\sigma}\end{aligned} \tag{22e}$$

To complete the problem statement, periodicity conditions are imposed at the inlets and outlets of the unit cell domain:

$$\tilde{c}_{A\sigma}(\mathbf{r}+\mathbf{l}_i)=\tilde{c}_{A\sigma}(\mathbf{r}),\quad i=1,2,3 \tag{22f}$$

$$\tilde{c}_{A\eta}(\mathbf{r}+\mathbf{l}_i)=\tilde{c}_{A\eta}(\mathbf{r}),\quad i=1,2,3 \tag{22g}$$

$$\tilde{c}_{A\beta}(\mathbf{r}+\mathbf{l}_3)=\tilde{c}_{A\beta}(\mathbf{r}) \tag{22h}$$

Finally, the concentration deviations are bounded by the average constraints:

$$\langle\tilde{c}_{A\sigma}\rangle^\sigma=0,\quad\langle\tilde{c}_{A\eta}\rangle^\eta=0,\quad\langle\tilde{c}_{A\beta}\rangle^\beta=0 \tag{22i}$$

Due to the linearity of the above boundary-value problem, the principle of superposition is applied so that its formal solution can be written in terms of the source terms as follows ($j=\sigma,\eta,\beta$):

$$\tilde{c}_{Aj}=\mathbf{b}_j\cdot\nabla\langle c_A\rangle+s_j\langle c_A\rangle \tag{23}$$

Here, the closure variables $\mathbf{b}_j$ and s_j, map the influence of each source onto $\tilde{c}_{Aj}$. Certainly, it may be argued that the derivations provided here are restricted to conditions in which the local equilibrium assumption is applicable and that other more robust alternatives should be considered as well. While this is certainly an appealing point that deserves deep discussion, in this work the local-equilibrium assumption is adopted with the intention of providing a first modeling approach that does not bring potential unnecessary complexities.

With this solution available, it is now possible to redirect the attention to the unclosed model given by equations (20). Adding these equations and taking into account the assumption of local mass equilibrium gives rise to the following unclosed average equation:

$$\begin{aligned}&\left(\varepsilon_\sigma+\varepsilon_\eta+\varepsilon_\beta\right)\frac{\partial\langle c_A\rangle}{\partial t}+\nabla\cdot(\langle c_A\rangle\langle\mathbf{v}\rangle_\sigma)+\nabla\cdot(\langle c_A\rangle\langle\mathbf{v}_\eta\rangle_\eta)\\&+\nabla\cdot(\langle c_A\rangle\langle\mathbf{v}_\beta\rangle_\beta)+\nabla\cdot(\langle\tilde{c}_{A\sigma}\mathbf{v}^\sigma\rangle_\sigma)+\nabla\cdot(\langle\tilde{c}_{A\eta}\mathbf{v}_\eta\rangle_\eta)\\&+\nabla\cdot(\langle\tilde{c}_{A\beta}\mathbf{v}_\beta\rangle_\beta)=\nabla\cdot\Big(\mathbf{D}^*\cdot\nabla\langle c_A\rangle\varepsilon_\sigma+\mathscr{D}_{A\eta}\nabla\langle c_A\rangle\varepsilon_\eta\\&+\mathscr{D}_{A\beta}\nabla\langle c_A\rangle\varepsilon_\beta\Big)+\nabla\cdot\left[\mathbf{D}^*\cdot\left(\frac{1}{V}\int_{\mathscr{A}_\sigma}\mathbf{n}_{\sigma\beta}\tilde{c}_{A\sigma}\,dA\right)\right.\\&\left.+\frac{\mathscr{D}_{A\eta}}{V}\int_{\mathscr{A}_\eta}\mathbf{n}_\eta\tilde{c}_{A\eta}\,dA+\frac{\mathscr{D}_{A\beta}}{V}\int_{\mathscr{A}_{\beta\sigma}}\mathbf{n}_{\beta\sigma}\tilde{c}_{A\beta}\,dA\right]\end{aligned} \tag{24}$$

Substitution of the formal solution, given in equations (23), into the above equation, gives rise to the final form of the upscaled model for species-*A* mass transport:

$$\frac{\partial \langle c_A \rangle}{\partial t} + \nabla \cdot (\langle c_A \rangle \mathbf{v}_{eff}) = \nabla \cdot \left(\mathbf{D}_{eff} \cdot \nabla \langle c_A \rangle \right) \tag{25}$$

The mathematical structure of this model is certainly anticipated; however, the effective velocity vector ($\mathbf{v}_{eff}$) and the total dispersion tensor ($\mathbf{D}_{eff}$) can be predicted from the closure variables fields and they are defined as follows:

$$\begin{aligned}(\varepsilon_\sigma + \varepsilon_\eta + \varepsilon_\beta)\mathbf{v}_{eff} &= \langle \mathbf{v}^\sigma \rangle^\sigma + \langle \mathbf{v}_\eta \rangle^\eta + \langle \mathbf{v}_\beta \rangle^\beta + \langle \mathbf{v}^\sigma s_\sigma \rangle^\sigma \\ &+ \langle \mathbf{v}_\eta s_\eta \rangle^\eta + \langle \mathbf{v}_\beta s_\beta \rangle^\beta - \mathbf{D}^* \cdot \left(\frac{1}{V} \int_{\mathscr{A}_\sigma} \mathbf{n}_{\sigma\beta} s_\sigma \, dA \right) \\ &- \frac{\mathscr{D}_{A\eta}}{V} \int_{\mathscr{A}_\eta} \mathbf{n}_\eta s_\eta \, dA - \frac{\mathscr{D}_{A\beta}}{V} \int_{\mathscr{A}_{\beta\sigma}} \mathbf{n}_{\beta\sigma} s_\beta \, dA \end{aligned} \tag{26a}$$

$$\begin{aligned}(\varepsilon_\sigma + \varepsilon_\eta + \varepsilon_\beta)\mathbf{D}_{eff} &= \mathbf{D}^* \varepsilon_\sigma + \mathscr{D}_{A\eta}\varepsilon_\eta \mathbf{I} + \mathscr{D}_{A\beta}\varepsilon_\beta \mathbf{I} \\ &+ \mathbf{D}^* \cdot \left(\frac{1}{V} \int_{\mathscr{A}_\sigma} \mathbf{n}_{\sigma\beta} \mathbf{b}_\sigma \, dA \right) + \frac{\mathscr{D}_{A\eta}}{V} \int_{\mathscr{A}_\eta} \mathbf{n}_\eta \mathbf{b}_\eta \, dA \\ &+ \frac{\mathscr{D}_{A\beta}}{V} \int_{\mathscr{A}_{\beta\sigma}} \mathbf{n}_{\beta\sigma} \mathbf{b}_\beta \, dA - \langle \mathbf{v}^\sigma \mathbf{b}_\sigma \rangle - \langle \mathbf{v}_\eta \mathbf{b}_\eta \rangle - \langle \mathbf{v}_\beta \mathbf{b}_\beta \rangle \end{aligned} \tag{26b}$$

With the above equations, the upscaled model for the ζ-region is complete and closed. The models derived here constitute the first part of the contribution of this work. The second contribution is the determination of the most favorable design and operating conditions. This is carried out in the following paragraphs.

5 Aerobic tank analysis

In this section the numerical solutions and analyses of the mass transport models for the aerobic tank are developed. This entails the separate simulation of species *A* and *B* through a similar procedure. The governing equations were numerically solved in the Comsol-Multiphysics 5.5 software. For the analysis of both species, a computational mesh with 1000 elements was used. This mesh was selected for resulting in a negligible error with respect to finer meshes (2000 elements), and leading to precise simulations.

The organization of this section is the following: Firstly, a parametric analysis is conducted to the dimensionless version of the models described in section 6. Through these analyses, the applicable interval of all the parameters and dimensionless numbers involved in the respective models is delimited. Secondly, the effect of these is evaluated over the response variable. The parametric analyses allow establishing the design and operating conditions that generate the best results in terms of species *A* consumption and species *B* concentration in the tank. All studies listed above are carried out assuming a single floc size. Thereafter, the effect that the distribution of floc sizes has on the consumption of LCFA and oxygen is studied.

Before proceeding to the parametric analysis, it is important to analyze the nature of the aerobic tank models. With the exception of the Michaelis-Menten term in the floc models, the governing equations for mass transport and reaction in the rest of the phases and regions are linear equations. One of the main attributes of linear models is the possibility of using the superposition principle. This implies that the output due to each input is independent of other inputs in the model, where each contribution refers to a different parameter. It is therefore possible to perform a series of simulations of a linear system examining each input separately. Thus, the output of the system for any combination of inputs is the sum of the outputs of the individual simulations (Gray & Gray, 2017). As for the Michaelis-Menten term, the numerical solutions for this type of model can be approximated by linear models of order one and zero (Valdés-Parada, Alvarez-Ramirez, & Ochoa-Tapia, 2005). This allows to proceed with the analysis of these equations in the same way as for a linear model and not requiring the analysis of the interaction between the different parameters involved.

5.1 *Species A*

In order to obtain the dimensionless mass transport equations for species *A*, the following definitions are introduced:

$$D_A^* = \frac{D_A}{\mathscr{D}_{A\beta}},\ R_f = max(R_j),\ R_j^* = \frac{R_j}{R_f},\ r^* = \frac{r}{R_f},\ t_A^* = \frac{t_A}{t_{D_A}},$$

$$t_{D_A} = \frac{R_f^2}{\mathscr{D}_{A\beta}},\ c_A^{\eta *} = \frac{c_A^\eta}{c_\lambda},\ c_{A\eta e}^* = \frac{c_{A\eta e}}{c_\lambda},\ c_{A\omega j}^* = \frac{c_{A\omega j}}{c_\lambda},$$

$$\alpha_{P_A}^* = \frac{\alpha_{P_A}}{c_\lambda},\ \mu_{AP_Aj}^* = \frac{\mu_{AP_Aj} t_{D_A}}{c_\lambda},\ \varepsilon_\eta = \frac{V_\eta}{V},\ \dot{Q}_{e\eta}^* = \frac{\dot{Q}_{e\eta} t_{D_A}}{V},$$

$$\dot{Q}^*_{s\eta} = \frac{\dot{Q}_{s\eta} t_{D_A}}{V},\ \phi^2_{\lambda\eta} = \frac{k_{\lambda\eta} R_f}{\mathscr{D}_{A\beta}},\ a^*_{\eta\lambda} = \frac{A_{\eta\lambda} R_f}{V},$$

$$a^*_{A\eta\omega j} = \frac{A_{\eta\omega j} R_f}{V},\ Bi_{Aj} = \frac{k^{\eta\omega}_{Aj} R_f}{\mathscr{D}_{A\beta}} \quad (27)$$

where * is employed to denote the dimensionless nature of each quantity. R_f is the maximum floc radius. D^*_A is the ratio between the effective diffusivity and the molecular diffusion coefficients for species A. t^*_A is the dimensionless time and t_{D_A} is the characteristic diffusion time, for species A. Additionally, Bi_{Aj} represents the Biot number for species A between the η and ω regions at its j-th size, and $\phi^2_{\lambda\eta}$ is defined as the Thiele modulus at the boundary between the λ and η zones.

Once the dimensionless model is obtained, the interval values for every parameter and dimensionless number required for species A model were determined. These are reported in table 1.

Given the absence of specific bibliographic references for biological systems of this type, chemical/biological reactor references were further limited by evaluating simulations within the range of values reported. Therefore, the resulting intervals shown for the different dimensionless numbers[1] were fixed in agreement with the literature. In contrast, the thermodynamic equilibrium constant (K^*_A) was assumed equal to 1, limiting the simulations to the particular case where both intracellular and extracellular concentrations inside the flocs are in equilibrium.

The purpose of the aerobic tank is to carry out the maximum possible oxidation of LCFA. The remaining substrate becomes the feed of the membrane tank, as it is carried with the η-region. For this reason, the response variable for the following analysis is the concentration of species A in the η-region. In order to quantify the magnitude of the variation of this response variable during the stationary phase, a parametric sweep was executed. This study enables not only the identification of the parameters to which the model is more sensible, but also the recognition of the type of effect produced over the response variable. The result of these parametric sweeps are shown in figure 4. It can be noticed that the effect generated by each parameter varies throughout its evaluated domain. In order to quantify the impact and compare between parameters, the slope of each curve was used. As seen in table 2, the classification of the parameters

Table 1: Species A parameters intervals.

Parameter	Min	Max	Reference
Bi_A	0.1	10	Valdés-Parada et al. (2005)
$\phi^2_{\lambda\eta}$	0.1	2	Valdés-Parada et al. (2005); Villadsen (2016)
$a^*_{\eta\omega}$	0.1	1	
$a^*_{\eta\lambda}$	0.1	1	
ε_e	0.1	1	Chu and Lee (2004a); Wood and Whitaker (2000)
ε_{P_A}	0.1	$1-\varepsilon_e-\varepsilon_{N_A}$	
K^*_A	1		
$\mu^*_{P_A}$	1×10^{-6}	9	Hsu et al. (1983); Nakhla et al. (2006)
$\alpha^*_{P_A}$	1×10^{-3}	9	Javed et al. (2018); Ji, Chen, Zhang, Lin, and Wei (2015)
ε_η	0.6	1	
$\dot{Q}^*_e$	3×10^{-5}	5×10^{-5}	(GE, 2014)
k	0.25		Wood and Whitaker (2000)

---

[1] *i.e.*, the Biot number at the boundary between the flocs and the η-region (Bi_A), the Thiele modulus at the boundary between the oil phase and the liquid region ($\phi^2_{\lambda\eta}$), the interfacial area between the η-region and the flocs ($a^*_{\eta\omega}$), the interfacial area between the η-region and the oil phase ($a^*_{\eta\lambda}$), the volumetric fraction of cells that consume LCFA (ε_{P_A}) and the volumetric fraction of the η-region with respect to the total volume of the aerobic tank (ε_η).

was done according with the magnitude order of the maximum change in slope, where substantial effect of the parameter corresponds to a magnitude order of 10^2 and minimum effect is equivalent to a magnitude order of 10^{-2}. This analysis was performed within the complete parameters domain, but it is reported for the magnitude interval where the effect was more significant (according to the third column). Furthermore, as the magnitude of the parameters increase, it results in either a negative or positive effect over the response variable, evidenced by the slope sign. This helps to understand the intervals in which the system is more sensible, and contributes to the magnitude selection of the design and operational conditions to favor species A oxidation. Parameters such as Bi_A and $\alpha_{P_A}^*$ generate very small changes on the concentration of species A, while the most influencing factors that contribute to the concentration of LCFA in the η-region are $a_{\eta\omega}^*$ (interfacial area per unit volume of the flocs), ε_e (proportion of the floc volume that represents the extracellular matrix) and ε_{P_A} (volumetric fraction of the cells that are capable of oxidizing LCFA with respect to those unable). This reflects the importance of floc quality in the operation of these bioreactors.

Once the parameters interval is established, and quantified the repercussion of their variation, it proceeds the selection of the magnitude that allows representing the phenomenon that takes place in the aerobic tank. The parameter values, as well as the result for the species A concentration dynamics,

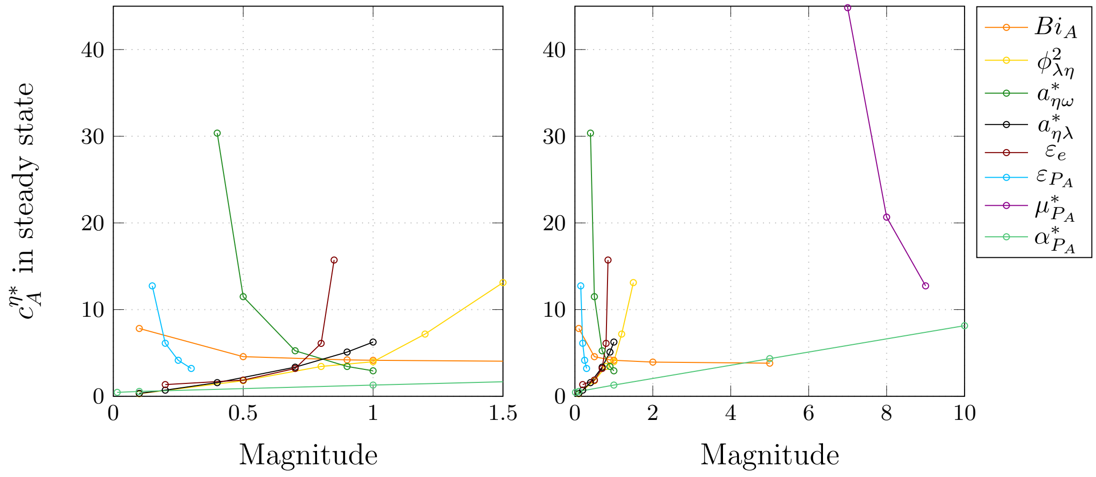

Fig. 4: Analysis of the effect generated by the variation of each parameter over the dependent variable.

Table 2: Parameter effect size for species A.

Parameter	**Maximum change in slope**	**Condition of maximum change**
$a_{\eta\omega}^*$	-188.7	0.6–0.8
ε_e	192.28	0.7–0.8
ε_{P_A}	-132.4	0.2–0.3
$\mu_{P_A}^*$	-81.68	$1x10^{-6}$–9
$\phi_{\lambda\eta}^2$	19.79	1–2
$a_{\eta\lambda}^*$	11.54	0.8–1
$\alpha_{P_A}^*$	0.76	$1x10^{-3}$–9
Bi_A	-0.01	0.1–0.5

are shown in figure 5. Here, initial dimensionless concentration inside the flocs was fixed at 0.05. With the passage of time, the concentration dynamics exhibit a slight change in slope due to the increasing transport rate to finally oxidize this excess of LCFA and find steady conditions around the dimensionless time $t^* = 6$. The same tendency is observed in the flocs interfacial dimensionless concentration. In the η-region, the concentration of dissolved LCFA decreases following a sigmoidal pattern due to the consumption taking place inside the flocs, until finding a simultaneous point of stability with the average concentration inside of the flocs and at their boundary. The final value of the dimensionless concentration of LCFA is 0.17 in the liquid region.

According to the literature, MBRs, and in general, systems involving flocular biomass, do not contain a single and uniform floc size, but rather have a size distribution (Chu & Lee, 2004b; Delgado, Villarroel, Gonzalez, & Morales, 2011; Shen et al., 2015; Spérandio, Masse, Espinosa-Bouchot, & Cabassud, 2005; Wu, He, & Zhang, 2012). To generate the size distribution in the present work, six different sizes were selected, and considering the percentage of the volume reported for each of them, the distribution was incorporated into the simulation program. The result is shown in figure 6. The average concentration of each floc radius is plotted here, where the largest floc size is 55 μm and the smallest one is 5 μm.

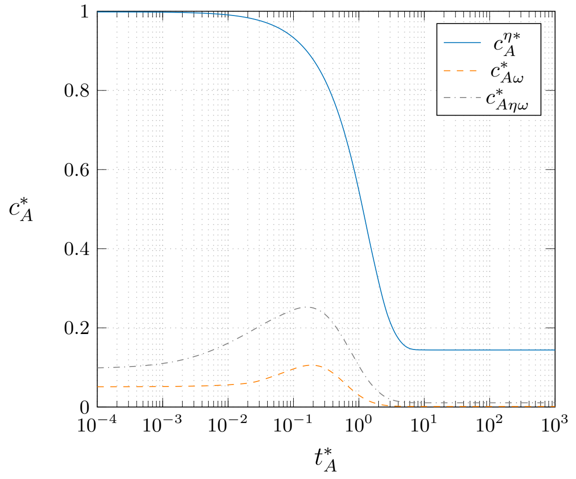

Fig. 5: Dimensionless concentration of species A as function of the dimensionless operating time. $Bi_A = 1$, $\phi_{\lambda\eta}^2 = 0.15$, $a_{\eta\omega}^* = 0.9$, $a_{\eta\lambda}^* = 0.8$, $\varepsilon_e = 0.7$, $\varepsilon_{P_A} = 0.25$, $K_A^* = 1$, $\mu_{P_A}^* = 9$, $\alpha_{P_A}^* = 0.003$, $\varepsilon_\eta = 0.85$, $\dot{Q}_e^* = 0.00003$, $k = 0.25$. Initial conditions: $c_{A0}^{\eta *} = 1$, $c_{A\omega j0}^* = 0.05$.

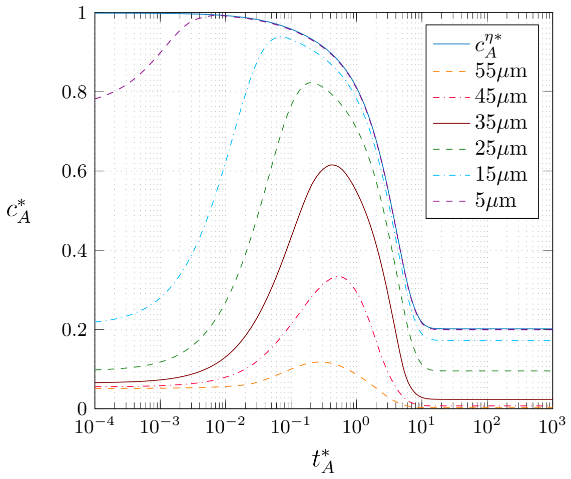

Fig. 6: Dimensionless concentration of species A as function of the dimensionless operating time, considering floc size distribution. $Bi_A = 1$, $\phi_{\lambda\eta}^2 = 0.15$, $a_{\eta\omega}^* = 0.9$, $a_{\eta\lambda}^* = 0.8$, $\varepsilon_e = 0.7$, $\varepsilon_{P_A} = 0.25$, $K_A^* = 1$, $\mu_{P_A}^* = 9$, $\alpha_{P_A}^* = 0.003$, $\varepsilon_\eta = 0.85$, $\dot{Q}_e^* = 0.00003$, $k = 0.25$. Initial conditions: $c_{A0}^{\eta *} = 1$, $c_{A\omega j0}^* = 0.05$.

As the radius of the flocs decreases, the average dimensionless concentration of the LCFA within them is higher, showing a low oxidation capacity of this species. As can be seen and comparing with figure 5, the average LCFA consumption among all flocs decreases. This can be attributed to the fact that when defining the size distribution, flocs smaller than the one initially contemplated (55 μm) are incorporated. In synergy, a lower consumption of LCFA occurs when it is considered that not all flocs are of the largest floc size.

This concludes the analysis of the dynamics of species A concentration in the aerobic tank. These results will be used as input values for the simulations presented in section 6. In the following section the analysis of the dynamics of the oxygen concentration within the aerobic tank is shown.

5.2 *Species B*

To begin the analysis for this chemical species, it is convenient to recast the model in terms of the following dimensionless definitions:

$$D_B^* = \frac{D_B}{\mathscr{D}_{B\beta}},\ r^* = \frac{r}{R_f},\ t_B^* = \frac{t_B}{t_{D_B}},\ t_{D_B} = \frac{R_f^2}{\mathscr{D}_{B\beta}},\ c_B^{\gamma *} = \frac{c_B^\gamma}{c_{B\gamma d}},$$

$$c_B^{\eta *} = \frac{c_B^\eta}{c_{B\gamma d}},\ c_{B\omega j}^* = \frac{c_{B\omega j}}{c_{B\gamma d}},\ \alpha_{P_B}^* = \frac{\alpha_{P_B}}{c_{B\gamma d}},\ \mu_{BP_B j}^* = \frac{\mu_{BP_B j} t_{D_B}}{c_{B\gamma d}},$$

$$\varepsilon_\eta = \frac{V_\eta}{V},\ \varepsilon_\gamma = \frac{V_\gamma}{V},\ \dot{Q}^*_{e\eta} = \frac{\dot{Q}_{e\eta} t_{D_B}}{V},\ \dot{Q}^*_{s\eta} = \frac{\dot{Q}_{s\eta} t_{D_B}}{V},$$
$$\dot{Q}^*_{d\gamma} = \frac{\dot{Q}_{d\gamma} t_{D_B}}{V},\ \dot{Q}^*_{sup\gamma} = \frac{\dot{Q}^*_{sup\gamma} t_{D_B}}{V},\ Bi_{\gamma\eta} = \frac{k_{\gamma\eta} R_f}{\mathscr{D}_{B\beta}},$$
$$Bi_{Bj} = \frac{k^{\eta\omega}_{Bj} R_f}{\mathscr{D}_{B\beta}},\ a^*_{\eta\gamma} = \frac{A_{\eta\gamma} R_f}{V},\ a^*_{B\eta\omega j} = \frac{A_{\eta\omega j} R_f}{V} \tag{28}$$

Here Bi_{Aj} represents the Biot number for species A between the η and ω regions at its j-th size, and $Bi_{\gamma\eta}$ is the Biot number between the γ and the η zones.

Considering the above definitions, numerical simulations of the species B model were developed. First, the values of the parameters were delimited. Table 3 shows the lower and upper limits for the magnitude of each of the parameters required to carry out the numerical simulations of oxygen in the aerobic tank. It can be noted that some of these have the condition that they must adopt the same range of values as for species A, this is applied to shared parameters and to avoid interfering with the best conditions for LCFA degradation.

As shown with species A, it is necessary to implement an analysis to evaluate the magnitude of each parameter that allows representing the phenomenon of oxygen consumption in the aerobic tank. To facilitate this, the results of the effect size estimation are shown below. Figure 7 shows curves for the change generated in the dependent variable according to the variation of each parameter. It is possible to note in table 4, that the parameters that produce the greatest change in concentration are the volumetric air flow rate ($\dot{Q}^*_d$) and the maximum specific oxygen consumption rate ($\mu^*_{P_B}$). For this species, there is a greater number

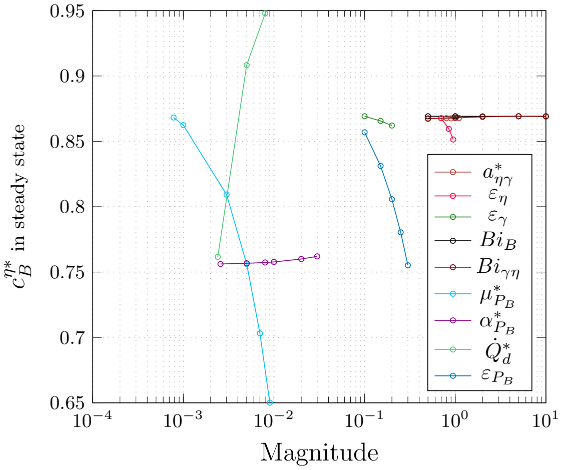

Fig. 7: Analysis of the effect generated by the variation of each parameter over the dependent variable.

Table 3: Species B parameters intervals.

Parameter	Min	Max	Reference
$a^*_{B\eta\omega}$	0.1	1	Limited to 0.9 by species A
$a^*_{\eta\gamma}$	0.1	1	Das, Bandopadhyay, Parthasarathy, and Kumar (1985)
Bi_B	0.1	10	Valdés-Parada et al. (2005)
$Bi_{\gamma\eta}$	0.1	10	Valdés-Parada et al. (2005)
ε_e	0.1	1	Limited to 0.7 by species A
ε_{P_B}	0.1	1-ε_e	
K^*_B	1		
$\mu^*_{P_B}$	1×10^{-5}	0.9	Garcia-Ochoa, Gomez, Santos, and Merchuk (2010)
$\alpha^*_{P_B}$	1×10^{-3}	0.09	Khakpour et al. (2017); Mines (2019)
$\dot{Q}^*_e$	3×10^{-5}	5×10^{-5}	Limited to 0.0003 by species A
k	0.25		Wood and Whitaker (2000)
ε_η	0.6	1	Limited to 0.85 by species A
$\dot{Q}^*_d$	1×10^{-3}	0.024	(Moilanen, Laakkonen, & Aittamaa, 2005)
ε_γ	0.1	0.4	(Das et al., 1985)

of parameters that have practically no effect on the response variable, unlike for species *A*. These parameters are: the volumetric fraction of the γ-phase in the reactor (ε_γ), the interfacial area per unit volume between the η-region and the γ-phase ($a^*_{\eta\gamma}$), the Biot number at the boundary between the flocs and the η-region (Bi_B) and the Biot number between the η-region and the γ-phase ($Bi_{\eta\gamma}$). For this species, the range of magnitudes where the parameters generate their greatest effect is not shown, due to the fact that throughout its domain the slope is practically constant.

Table 4: Parameter effect size for species *B*.

Parameter	Maximum change in slope
$\dot{Q}^*_d$	56.42
$\mu^*_{P_B}$	-26.52
ε_{P_B}	-0.5
$\alpha^*_{P_B}$	0.19
ε_γ	-0.7
$a^*_{\eta\gamma}$	0.00037
Bi_B	0.0004
$Bi_{\eta\gamma}$	0.0019

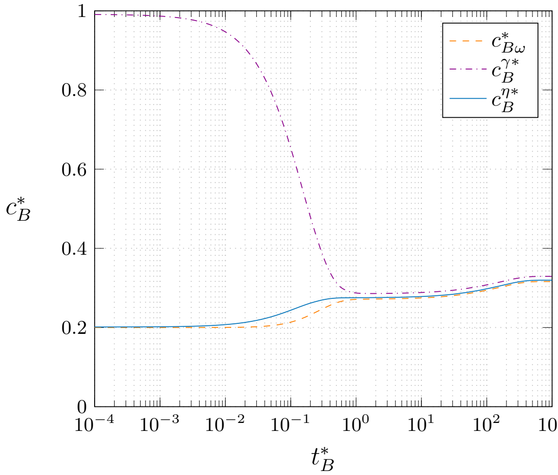

Fig. 8: Dimensionless concentration of species *B* as function of the dimensionless operating time. $a^*_{B\eta\omega} = 0.9$, $a^*_{\eta\gamma} = 0.7$, $Bi_B = 5$, $Bi_{\gamma\eta} = 1$, $\varepsilon_e = 0.7$, $\varepsilon_{P_B} = 0.28$, $K^*_B = 1$, $\mu^*_{P_B} = 0.08$, $\alpha^*_{P_B} = 0.00257$, $\varepsilon_\eta = 0.85$, $\dot{Q}^*_e = 0.00003$, $k = 0.25$, $\varepsilon_\gamma = 0.12$, $\dot{Q}^*_d = 0.01$. Initial conditions: $c^{\gamma*}_{B0} = 1$, $c^{\eta*}_{B0} = 0.2$, $c^*_{B\omega j0} = 0.2$.

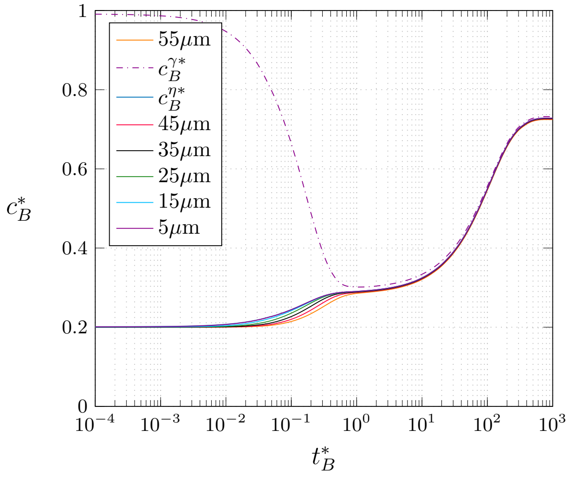

Fig. 9: Dimensionless concentration of species *B* as function of the dimensionless operating time, considering floc size distribution. $a^*_{B\eta\omega} = 0.9$, $a^*_{\eta\gamma} = 0.7$, $Bi_B = 5$, $Bi_{\gamma\eta} = 1$, $\varepsilon_e = 0.7$, $\varepsilon_{P_B} = 0.28$, $K^*_B = 1$, $\mu^*_{P_B} = 0.08$, $\alpha^*_{P_B} = 0.00257$, $\varepsilon_\eta = 0.85$, $\dot{Q}^*_e = 0.00003$, $k = 0.25$, $\varepsilon_\gamma = 0.12$, $\dot{Q}^*_d = 0.01$. Initial conditions: $c^{\gamma*}_{B0} = 1$, $c^{\eta*}_{B0} = 0.2$, $c^*_{B\omega j0} = 0.2$.

During the aerobic tank operation, the objective is to maintain the dissolved oxygen concentration stable at around 30% to avoid oxygen limitations (Wang & Zhong, 2007). It is possible to observe, in figure 8, the oxygen concentration of the γ-phase dropping since the start of aeration, and subsequently, reaching equilibrium with the η-region at around 30% saturation. Within the flocs, the concentration features a slight alteration but, at all times, it remains between 0.2 and 0.3.

As for the analysis of species *A*, it is important to consider the size distribution of the flocs at this point, due to the fact that this can affect the rate of oxygen consumption. Considering the same size distribution as for the LCFA, figure 9 is obtained. It is possible to note that due to the presence of smaller flocs (<55 μm in radius), the oxygen consumption is, on average, less than when the distribution of floc sizes is not considered. The analysis allows to conclude that the largest flocs consume the greatest amount of this chemical species; therefore, oxygen consumption analysis can always be performed using the largest floc size as a reference. In this way, there is sufficient oxygen supply so that the consumption of the carbon source is not limited.

5.3 *Best design and operating conditions*

From the analysis carried out in this section, the best design and operating conditions for the aerobic tank were identified. The design parameters are those that are established prior to the operation of the reactor and they cannot be modified once the process is started. On the contrary, the operating parameters are those that can be modified during the degradation of LCFA.

Based on this distinction, the best dimensionless design conditions for the aerobic tank are: Large interfacial areas between the liquid and the floc per unit volume ($a^*_{\eta\omega}$ and $a^*_{B\eta\omega}$), with values close to, but below, one. Similarly, it is recommended to have interfacial areas between the liquid region and the oil phase and between the liquid and the air bubbles per unit volume ($a^*_{\eta\lambda}$ and $a^*_{\eta\gamma}$, respectively) close to, but less than, one. This can be interpreted as flocs, micelles and bubbles, either small and/or in large quantities. The exact dimensionless values that generate the best operating conditions for the interfacial areas are: $a^*_{\eta\omega} = a^*_{B\eta\omega} = 0.9$, $a^*_{\eta\lambda} = 0.8$ and $a^*_{\eta\gamma} = 0.7$. A low hydrolytic rate is desired in the aerobic tank, which is determined by the Thiele modulus value and it is desirable to maintain it below one. According to the analysis, the recommended value is $\phi^2_{\lambda\eta} = 0.15$. It is important to mention that, although this is considered a design parameter, it is possible to modify it momentarily by the addition of hydrolytic enzymes, if that were the case. Regarding the quality of the flocs to be used, it is advantageous to operate with the presence of the largest possible cellular fraction and acclimatize the cells to grow with high LCFA contents to have high oxidative rates ($\mu^*_{P_A}$ close to 10) with low saturation constants ($\alpha^*_{P_A} \leq 10^{-3}$). For this reason, volumetric fractions for the extracellular matrix are recommended to be kept below 0.7 and volumetric fractions for cells that consume LCFA as high as possible (limited, of course, by the fraction of the extracellular matrix). The values used in this work correspond to $\mu^*_{P_A} = 9$, $\alpha^*_{P_A} = 0.003$, $\varepsilon_e = 0.7$ and $\varepsilon_{P_A} = 0.25$. For oxygen, there is no limitation for the degradation of LCFA as long as the dimensionless specific rate of consumption of this substrate and the saturation constant are lower or equal to 10^{-2}. In this study $\mu^*_{P_B} = 0.08$ and $\alpha^*_{P_B} = 0.00257$, were used. Due to the fact that it is an aerobic tank, the volumetric fraction of cells that consume oxygen is expected to be high ($\varepsilon_{P_B} = 0.28$ in this study), found far from zero and with an upper limit depending on the volumetric fraction representing the extracellular matrix. Finally, the liquid region inside the tank must represent the majority of the total volume (established in this study as $\varepsilon_\eta = 0.85$), so the volumetric fraction of air must be minor (established at $\varepsilon_\gamma = 0.12$). However, the change in the fraction of the liquid region does not represent large changes in the degradation of LCFA and oxygen consumption.

The best dimensionless operating conditions for the aerobic tank are given by: Low dimensionless volumetric feed flow rates for the reactor, of the order of 10^{-5}. As a result of this work, $\dot{Q}^*_e = 0.00003$ was established. Furthermore, it is desired to have low mass transport resistances between the liquid region and the flocs, both for the LCFA and for oxygen. This translates into values for the Biot numbers greater or equal than one, and according to the previous analysis they were fixed at $Bi_A = 1$ and $Bi_B = 5$, respectively. This is achieved by maintaining high agitation rates by high dimensionless volumetric air flows (of the order of 10^{-2}), using in this work $\dot{Q}^*_d = 0.01$. It is also desirable that mass transport resistances between the bubbles and the liquid region become minimal. This motivates recommending achieving Biot number values greater or equal than one ($Bi_{\eta\gamma} = 1$). Despite having obtained a single value as a result of this study, both for design and operating parameters, this does not mean that they cannot oscillate around these magnitudes when applied experimentally to a system.

The quantitative contributions of this work are expressed through parameters and dimensionless numbers. The specific dimensional value for each parameter depends on the configuration and operating conditions of the system under study. It is therefore possible to obtain dimensional values that satisfy what was found in this parametric analysis by using the definitions given in this section for the aerobic tank. In this way, dimensionless numbers and parameters can be used for any type of aerobic tank that meets the model assumptions detailed previously. Furthermore, making use of the results obtained, it is possible to detect, in advance, the sensitivity of the system under study (including physically existing systems) to changes in operating parameters. Moreover, the model solution allows determining the dynamics of the concentration, where stable phases and phases with drastic changes are identified. At the same time, with the numerical simulations, it is possible to determine operating times in which strict control of the reactor is necessary and predict the time in which the system reaches the steady state. These last two points can be used to facilitate operational decision-making in wastewater treatment plants.

6 Membrane tank analysis

In this section the parametric and numerical analysis of the membrane tank was developed. In order to achieve this, the section is organized in two parts: First, the parametric analysis of the mass transport of species A is conducted, and the intervals where the parameters can be used are reported. Second, the results for the 3D model of the membrane tank are shown, involving both momentum and mass transport, and corresponding to the most favorable transport conditions. Momentum transport was assumed quasi-steady with respect to mass transport. The latter is coupled to momentum transport but the opposite is not true.

Similarly to the aerobic tank, the dimensionless model for mass transport was programmed in Comsol-Multiphysics 5.5. For this purpose, the following dimensionless definitions are given:

$$
\begin{gathered}
c^*_{A\zeta} = \frac{c_{A\zeta}}{c_\lambda}, \quad c^*_{A\eta} = \frac{c_{A\eta}}{c_\lambda}, \quad c^*_{A\zeta 0} = \frac{c_{A\zeta 0}}{c_\lambda}, \quad c^*_{A\eta 0} = \frac{c_{A\eta 0}}{c_\lambda}, \\
\mathsf{D}^*_{ef} = \frac{\mathsf{D}_{ef}}{\mathscr{D}_{A\beta}}, \quad \mathscr{D}^*_{A\eta} = \frac{\mathscr{D}_{A\eta}}{\mathscr{D}_{A\beta}}, \quad t_D = \frac{\ell_c^2}{\mathscr{D}_{A\beta}}, \quad t^* = \frac{t}{t_D}, \\
\nabla^* = \nabla \ell_c, \quad \mathsf{H}^* = \frac{\mathsf{H}}{\ell_c^2}, \quad \mathbf{v}^*_{ef} = \frac{\mathbf{v}_{ef}}{v_{ref}}, \quad \mathbf{v}^*_{\eta} = \frac{\mathbf{v}_{\eta}}{v_{ref}}, \\
\mathbf{e}_{v_{ref}} = \frac{\mathbf{v}_{ref}}{v_{ref}}, \quad \mathbf{v}^*_{efsup} = \frac{\mathbf{v}_{efsup}}{v_{ref}}, \quad \langle \mathbf{v} \rangle^* = \frac{\langle \mathbf{v} \rangle}{v_{ref}}, \\
\mathscr{P}^*_{\eta} = \frac{\mathscr{P}_{\eta}}{\rho_\eta v_{ref}^2}, \quad \mathscr{P}^*_{atm} = \frac{\mathscr{P}_{atm}}{\rho_\eta v_{ref}^2}, \quad \langle \mathscr{P} \rangle^* = \frac{\langle \mathscr{P} \rangle}{\rho_c v_{ref}^2}, \\
Re = \frac{\rho_\eta v_{ref} \ell_c}{\mu}, \quad Re_c = \frac{\ell_c \rho_c v_{ref}}{\mu_{prom}}, \quad Pe = \frac{v_{ref} \ell_c}{\mathscr{D}_{A\beta}}, \\
Bi_{\eta\zeta} = \frac{k^\zeta \ell_c}{\mathscr{D}_{A\beta}}, \quad Bi_{\zeta o} = \frac{k^o \ell_c}{\mathscr{D}_{A\beta}}
\end{gathered}
\tag{29}
$$

where t_D is the characteristic time of diffusion for the species A in the membrane tank, v_{ref} is the reference speed, which is the maximum reached within the system and $\mathbf{e}_{vref}$ is a unit vector in the direction of the reference velocity. Also, Pe is the Péclet number and $\mathscr{P}_{atm}$ is the atmospheric pressure. As it can be noted, two different Reynolds numbers have been defined, one for the η-region (Re) and one for the ζ-region (Re_c). This means that the movement of the fluid in and out of the ultrafiltration cassettes may have different flow regimes due to the different ratios of inertial and viscous contributions.

The mathematical models corresponding to the η-region and the ζ-region were numerically solved using the laminar flow and the Darcy-Brinkman modulus, respectively, which are available in the Comsol software. The reason to adopt the Darcy-Brinkman module, instead of the Darcy module, is due to the fact that the average velocity within the ultrafiltration cassettes undergoes spatial changes near their boundaries, which cannot be predicted using simply Darcy's law. As a first approximation, the resistance to momentum transport between the η and the ζ regions is not considered. This leads to maximum values of convective mass transport, with respect to diffusive transport as it will be clearly evidenced later. Furthermore, due to the lack of consensus on the best alternative for the *a priori* definition of the jump coefficient α in the Beavers-Joseph boundary condition, it is advantageous to reduce this degree of freedom, which, in addition, facilitates numerical simulations. However, the foregoing does not represent an impediment for the analysis of the transport mechanisms of the membrane tank, and it does not have a major impact on the mass transport of the species within the ultrafiltration cassettes, as the findings indicate.

It is important to mention that the results reported here were obtained using a computational mesh calibrated for fluid dynamics with 72,552 elements. This mesh, compared to finer meshes (145,055 elements), generates less than 2% error in the results; therefore is considered sufficiently accurate. It should also be addressed that the dimensionless values for the effective diffusivity coefficient (D^*) and the effective dispersion tensor (D_{eff}) of species A were estimated from the Rayleigh (1892) model, incorporating a correction factor (Whitaker, 1999) due to the existing convection in the system. Moreover, the dimensionless form of the apparent permeability coefficient (H^*) was estimated through the equation proposed by Chai, Lu, Shi, and Guo (2011); because of this, H^* is reduced to the isotropic permeability tensor and it depends of the volumetric fraction of the total fluid in the ultrafiltration cassettes.

All the models, with the exception of the one that governs the fluid outside the cassettes (Navier-Stokes equation), are linear equations. However, under low Reynolds flows (creeping flows), it is possible to simplify the parametric analysis. For this purpose, a comparative study between the creeping and the laminar flow modules from Comsol Multiphysics was performed. The magnitude of the velocity was measured at different points of the reactor: areas near the feed port, between the ultrafiltration cassettes, and near the side surfaces of the tank. In addition, the flow patterns defined by the velocity streamlines resulting from both numerical solutions were compared. The results were quite similar in terms of direction, suggesting the predominance of convective mass flux. In the rest of the zones, the lesser degree of similarity between the results obtained is not important because convection is not the principal mass transport mechanism of species A. Based on the above, it can be concluded that the flow within the membrane tank is predominantly creeping and therefore both the creeping and laminar flow modulus can be used for these numerical simulations. Since this model under creeping flow conditions is linear, it follows that all equations governing transport both inside and outside the ultrafiltration cassettes can be analyzed as linear models.

Through the parametric analysis, developed similarly to the one applied to the aerobic tank, the parameters interval was established as shown in table 5. After having analyzed the dimensionless parameters and numbers involved in the mathematical model, it is possible to select the values that generate a better representation of the physical system being modeled. Unlike the aerobic tank, an effect size study is not presented here, since few parameters truly contribute to an increase or decrease in the concentration of species A from the tank. Under constant geometry and fluid properties, the most important parameters identified are the Biot numbers that define the permeability of the membrane; as well as the Péclet number, on which depends the speed of the fluid responsible for the convective species mass transport. The most favorable conditions are high resistance to mass transport at the hollow fibers surface, as well as low resistance to mass transport between the hollow fibers and the permeate. Furthermore, it is necessary to operate at low flow rates to avoid promoting convective transport into the cassettes, which is reflected in small values for the Péclet number (*i.e.*, $Pe \leq 1$). All of the above is to obtain desirable values of the response variable, which means outlet concentrations of the chemical species in the permeate that help complying with environmental regulations.

The values for the parameters are presented in figure 10 and the dynamics of the dimensionless concentration of the LCFA as a function of time is plotted. This result was obtained after considering the coupled nature of both aerobic and membrane tanks, where the dimensionless concentration of species A in the η-region at the feed of the membrane tank corresponds to the dimensionless average concentration of the η-region in the aerobic tank ($c_A^{\eta *} = 0.17$). As can be seen, once the tank is fed with the effluent from the aerobic tank, the dimensionless average concentration of species A in each of the ultrafiltration cassettes permeate increases. This starts at dimensionless time of $t^* = 10$ and resembles a sigmoidal curve,

Table 5: Validity interval of parameters for the membrane tank.

Parameter	Min	Max	Reference
$\varepsilon_{\beta\sigma}$	0.6	0.9	Farahani, Rabiee, Vatanpour, and Borghei (2015); Zheng, Wang, Yang, and Cui (2006)
Pe	0.01	3	Ding, Liu, and Xu (2013); Skoneczny and Cioch (2018)
$Bi_{\eta\zeta}$	0.1	1	Valdés-Parada et al. (2005)
$Bi_{\zeta o}$	1	7	Valdés-Parada et al. (2005)
ε_f	0.4	0.85	
ε_σ	0.1	$1-\varepsilon_f$	
ε_γ	0.1	1	
ε_l	0.1	$1-\varepsilon_\sigma-\varepsilon_\gamma$	
Re	10^{-3}	$< 10^2$	Limited by the Pe
Re_c	10^{-3}	$< 10^1$	Limited by the Re
$c^*_{A\eta e}$	0.17		Limited by the aerobic tank
c^*_{Ao}	<0.1		Liu, Nakhla, and Bassi (2004); Nakhla, Al-Sabawi, Bassi, and Liu (2003) Acharya, Nakhla, Bassi, and Kurian (2006); Kurian, Nakhla, and Bassi (2006)

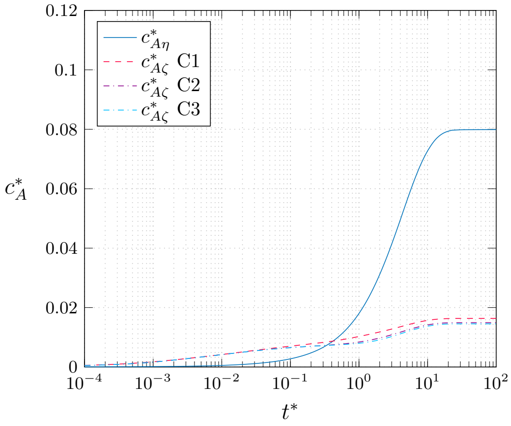

Fig. 10: Dynamics of the dimensionless concentration of the species A as a function of the dimensionless operating time in the membrane tank. $Bi_{\eta\zeta} = 0.1$, $Bi_{\zeta o} = 7$, $Pe = 1$, $\varepsilon_{\beta\kappa} = 0.7$, $\varepsilon_\sigma = 0.6$, $\varepsilon_l = 0.3$, $\varepsilon_f = 0.4$, $c^{\eta*}_{Ae} = 0.17$, $c^*_{A\eta e} = 0.17$. Initial conditions: $c^*_{A\eta 0} = 0$, $c^*_{A\zeta 0} = 0$.

which reaches the steady state before $t^* = 100$. In turn, the dimensionless concentration in the η-region outside the cassettes remains very close to zero and shoots up between $t^* = 0.1$ and $t^* = 10$, to finally reaching the steady state at the same time as the concentration inside the effective media. The final dimensionless concentrations at the permeate of the cassettes are very similar and are around 0.015, while the dimensionless concentration outside of them is 0.08. This corresponds to the reported efficiencies for MBRs, and allows producing effluents with characteristics close to those required by Mexican norms for national waters discharge (SEMARNAT, 2018).

6.1 *3D modeling of the membrane tank*

To complement the membrane tank analysis, the following paragraphs show the results of the velocity streamlines, total flux and gradient of the concentration of LCFA. The selected time shown for the total flux and concentration gradient corresponds to $t^* = 100$, where, according to figure 10, the system is already operating under steady state conditions. The dynamics of previous times is not shown, however, a summary of the phenomena taking place is provided.

In figure 11 the velocity streamlines within the membrane tank are plotted. It is possible to notice a higher speed at the feeding of the tank, being its dimensionless magnitude the maximum. Once the fluid enters the tank and moves away from the feed port, the velocity decreases. The velocity streamlines show two main patterns: A descending pattern, which mobilizes the fluid from the tank surface towards the upper-middle part of the ultrafiltration cassettes. A second pattern exhibits mobilization from the inlet and to the distal parts of the tank, to later move towards the cassettes. Also, it can be noticed a fluid stream that moves transversely under the three cassettes. These streamlines, by intercepting the rear wall of the tank, create an upward flow throughout the rear of the tank. The aforementioned streamlines eventually enter the cassettes through all of their surfaces.

Similarly, velocity streamlines for the interior of the ultrafiltration cassettes are reported in figure 12. The patterns observed in the three cassettes are similar, especially the acceleration of the fluid at the top of the cassettes. This acceleration is due to the negative pressure exerted on the permeate during the filtration process, and that, at the exit of the hollow fibers, produces a more noticeable change in the fluid speed. Due to this pressure difference, the cassettes flow pattern is directed upwards at all times. It should be noticed that the maximum dimensionless velocity inside the cassettes is slower than on the outside of them.

Results for the total flux and the concentration gradient are presented below, which allow elucidation of the mass transport mechanisms taking place in the system. First, the total mass flux result is given. Through time, a defined pattern for the streamlines of total flux is developed. This pattern, when compared to the convective velocity streamlines (see figures 11

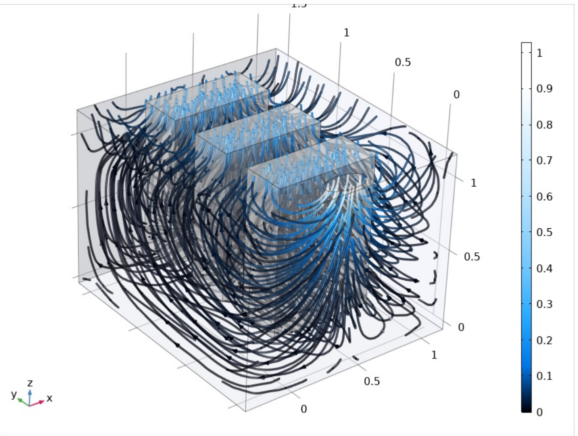

Fig. 11: Velocity streamlines inside the membrane tank. $Re = 1{\times}10^{-3}$, $Re_c = 5{\times}10^{-4}$, $\varepsilon_{\beta\kappa} = 0.7$, $\varepsilon_\sigma = 0.6$, $(\varepsilon_\eta + \varepsilon_\beta) = 0.3$, $(\varepsilon_\eta + \varepsilon_\beta + \varepsilon_\gamma) = 0.4$.

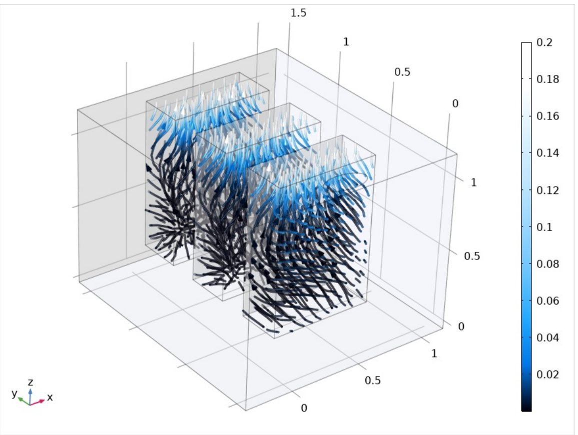

Fig. 12: Velocity streamlines inside the ultrafiltration cassettes of the membrane tank. $Re = 1 \times 10^{-3}$, $Re_c = 5 \times 10^{-4}$, $\varepsilon_{\beta\kappa} = 0.7$, $\varepsilon_\sigma = 0.6$, $(\varepsilon_\eta + \varepsilon_\beta) = 0.3$, $(\varepsilon_\eta + \varepsilon_\beta + \varepsilon_\gamma) = 0.4$.

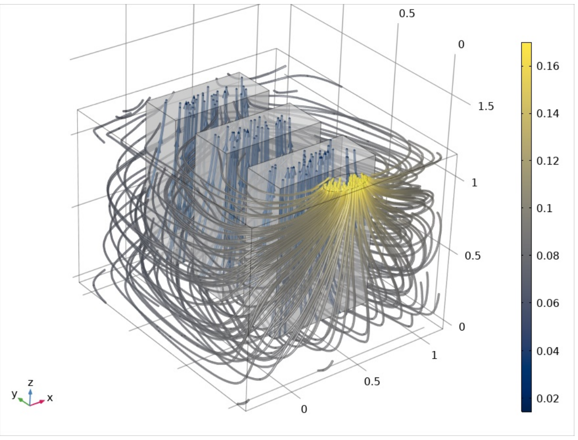

Fig. 13: Streamlines of the total flux inside the membrane tank, $t^* = 100$. $Bi_{\eta\zeta} = 0.1$, $Bi_{\zeta o} = 7$, $Pe = 1$, $\varepsilon_{\beta\kappa} = 0.7$, $\varepsilon_\sigma = 0.6$, $(\varepsilon_\eta + \varepsilon_\beta) = 0.3$, $(\varepsilon_\eta + \varepsilon_\beta + \varepsilon_\gamma) = 0.4$, $c_{Ae}^{\eta*} = 0.17$, $c_{A\eta e}^* = 0.17$. Initial conditions: $c_{A\eta 0}^* = 0$, $c_{A\zeta 0}^* = 0$.

and 12), provides the majoritarian mass transport mechanisms. Though not clear at initial times, from time $t^* = 1$ it can be noticed the main contributions of convective transport outside the ultrafiltration cassettes, mainly on the lower section of the membrane tank and proximal to the inlet, where the concentration of species A is maximum. Only in the upper section of the tank, the convective and the diffusive mass transport contribute equally. The above mechanisms are maintained until reaching the steady state conditions and the total flux streamlines are displayed in figure 13.

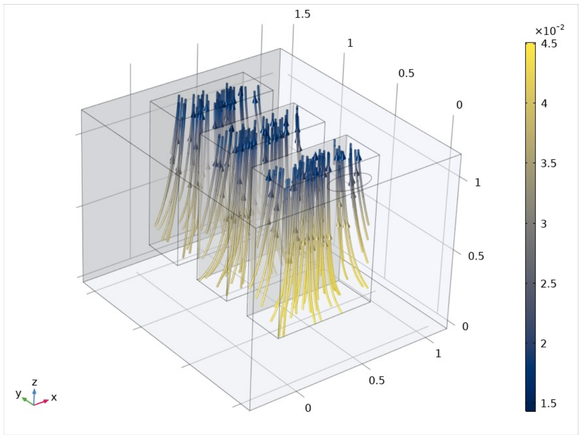

Fig. 14: Streamlines of the total flux inside the ultrafiltration cassettes of the membrane tank, $t^* = 100$. $Bi_{\eta\zeta} = 0.1$, $Bi_{\zeta o} = 7$, $Pe = 1$, $\varepsilon_{\beta\kappa} = 0.7$, $\varepsilon_\sigma = 0.6$, $(\varepsilon_\eta + \varepsilon_\beta) = 0.3$, $(\varepsilon_\eta + \varepsilon_\beta + \varepsilon_\gamma) = 0.4$, $c_{Ae}^{\eta*} = 0.17$, $c_{A\eta e}^* = 0.17$. Initial conditions: $c_{A\eta 0}^* = 0$, $c_{A\zeta 0}^* = 0$.

Inside the cassettes, diffusion represents the main mass transport mechanism. This is due to the lower speed of the fluid inside the cassettes with respect to the outside of them. However, convective transport becomes relevant in the upper section of the cassettes. In figure 14, the corresponding total mass flux streamlines inside the cassettes are reported at the same dimensionless time condition considered in the previous figure. These results show that under steady conditions, the effect of the negative pressure remains, evidenced by a domination of the diffusive mass transport in the z component, and to a lesser extent, in the x and y directions. The effect of the location of the feed port over the total mass flux is, in contrast, less evident in the three ultrafiltration cassettes. As for the magnitude of diffusive transport, in the z component of the cassettes it represents more than 93% of total mass transport domain-wide. In the middle and lower section it accounts for 98–99%, while in the upper zone it contributes to 93-98%. In the x component, the diffusion in the middle and lower section of all cassettes represents between 90 and 100% of the total mass flux, while in the region closest to the tank surface this percentage decreases in some zones, resulting in values above 50%. Only in the x component, and in the region of the cassette closest to the tank feed, does the ratio of diffusive transport to total flux drop to around 40%. For its part, in the y component, the low and middle sections of the cassettes retain the same proportions as in the x component; however, the upper part of the

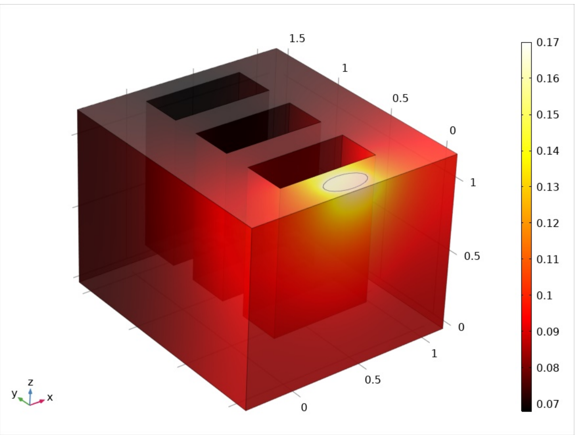

Fig. 15: Surface plot of the dimensionless concentration of species A inside the membrane tank, $t^* = 100$. $Bi_{\eta\zeta} = 0.1$, $Bi_{\zeta o} = 7$, $Pe = 1$, $\varepsilon_{\beta\kappa} = 0.7$, $\varepsilon_{\sigma} = 0.6$, $(\varepsilon_{\eta} + \varepsilon_{\beta}) = 0.3$, $(\varepsilon_{\eta} + \varepsilon_{\beta} + \varepsilon_{\gamma}) = 0.4$, $c_{Ae}^{\eta *} = 0.17$, $c_{A\eta e}^{*} = 0.17$. Initial conditions: $c_{A\eta 0}^{*} = 0$, $c_{A\zeta 0}^{*} = 0$.

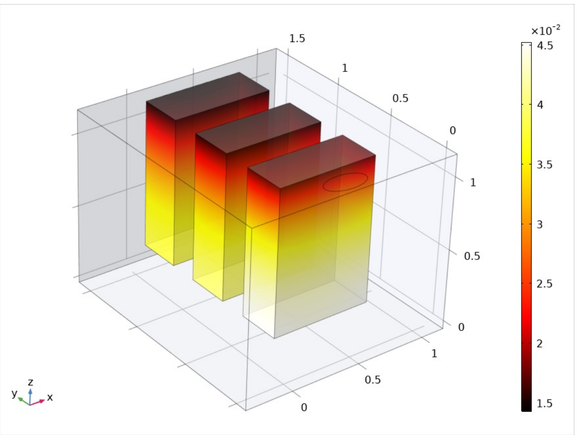

Fig. 16: Surface plot of the dimensionless concentration of species A inside the ultrafiltration cassettes of the membrane tank, $t^* = 100$. $Bi_{\eta\zeta} = 0.1$, $Bi_{\zeta o} = 7$, $Pe = 1$, $\varepsilon_{\beta\kappa} = 0.7$, $\varepsilon_{\sigma} = 0.6$, $(\varepsilon_{\eta} + \varepsilon_{\beta}) = 0.3$, $(\varepsilon_{\eta} + \varepsilon_{\beta} + \varepsilon_{\gamma}) = 0.4$, $c_{Ae}^{\eta *} = 0.17$, $c_{A\eta e}^{*} = 0.17$. Initial conditions: $c_{A\eta 0}^{*} = 0$, $c_{A\zeta 0}^{*} = 0$.

cassettes presents a lower contribution by diffusion in mass transport, with respect to the previously described component. In this area, a lower proportion of diffusive transport was observed, representing in most of the area, between 40 and 80% of the total mass flux.

In figures 15 and 16, surface plots corresponding to the spatial distribution of species A outside and inside the filtration cassettes are reported under steady-state conditions. It is possible to observe that there is still a marked concentration gradient of the chemical species throughout the tank. This gradient is probably formed due to the uptake generated by a pressure gradient in the first cassette. The LCFA are mostly retained here; therefore, the concentration of species A in the rear region of the tank is lower than that of the inlet. Furthermore, because the second cassette performs a similar action, at the back section of the tank the dimensionless concentration of the chemical species is already one order of magnitude smaller than that of the inlet.

As shown in figure 16, the concentration in the fluid external to the cassettes influences the saturation of these regions; therefore, the permeate concentration. This is mainly noticed in the first cassette, where the contact with greater quantities of species A favors the saturation, and to a lesser extent in the other two cassettes. A characteristic conserved through time is the higher saturation in the upper section of all the cassettes with respect to the rest of them; this is attributed to the location of the feeding port. Something that should be noted is that the average dimensionless concentration at the permeate of the cassettes is maintained at all times between 1.5×10^{-2} and 2×10^{-2} (which represents between 1.5 and 2% of the initial LCFA concentration in the aerobic tank). This corresponds to experimentally reported data for this type of reactors (Acharya, Nakhla, & Bassi, 2006a, 2006b; Kurian et al., 2005; Liu et al., 2003; Nakhla et al., 2006). The fat-reducing ability of MBRs (by up to 98%) results in approximate LCFA concentrations at the permeate outlet of less than 29.2 mg L^{-1}.

It is worth mentioning that the numerical simulations carried out in this work are computationally less demanding than those corresponding to CFD where an effective medium approach is not used to model transport inside the ultrafiltration cassettes. In this way, it can be said that the type of modeling developed in this work is more versatile than CFD type simulations, maintaining the essential information of the various scale levels of this multiphase system.

6.2 *Best design and operating conditions*

From the analysis carried out for the membrane tank, the best design and operating conditions were identified and those corresponding to design can be summarized as follows: It is desirable that the porosity of the medium that makes up the hollow fibers is high (about 0.75), while the volumetric fraction of the filter medium in the domain of the cassettes takes values around 0.6. Finally, because the fraction of filter medium in the ultrafiltration cassettes must be high, this limits the liquid fraction to be less than 0.5, using $\varepsilon_\eta + \varepsilon_\beta = 0.3$ in this work. When including the gas phase, the fluid fraction should not exceed 0.5 either; consequently, it was fixed in this study to be $\varepsilon_\eta + \varepsilon_\beta + \varepsilon_\gamma = 0.4$.

In addition, the best dimensionless operating conditions for the membrane tank were found to be: High resistances to mass transport between the liquid and the membrane, which correspond to Biot number values less than one and preferably close to zero (*i.e.*, $Bi_{\eta\zeta} = 0.1$). In addition, low mass transport resistances between the hollow fibers and the permeate are required, given by Biot number values greater or equal to one and lesser or equal to seven. This is related to the fluid velocity surrounding the cassettes, since the lower the degree of agitation, the greater the resistance to mass transport. The velocity is controlled indirectly through the Péclet number. Small magnitudes are preferable for it, less than or equal to 3 (in this analysis $Pe = 1$). By means of the Schmidt number, the values of the Pe limits the magnitude of the Reynolds number to values below 10^{-2} outside the ultrafiltration cassettes and below 10^{-1} inside them.

Conclusions

In this work, a mathematical model was derived to describe reaction and mass transport within membrane bioreactors. The model has the characteristic of filtering information from the microscopic scale to the reactor level.

The mathematical model for the aerobic tank consists of two equations for the transport and reaction of the LCFA, and three equations for oxygen; plus two continuity equations averaged across the tank. Given that the region where the most important changes in the LCFA and oxygen occur are the flocs, the information on the spatio-temporal changes of the species is preserved in the corresponding macroscopic equations. While in the other phases and regions the model only contemplates the temporary changes of the dependent variables.

The mathematical model derived for the membrane tank is composed of effective medium equations that describe the transport of mass and momentum in the ultrafiltration cassettes. From the scaling process, it is concluded that the macroscopic model for the mass transport of the LCFA, under the assumption of local mass equilibrium, is of the convection-dispersion type. Whereas, for momentum transport, the macroscopic model is Darcy's law type. These equations no longer distinguish between each component of the domain and have the advantage of incorporating predictable coefficients.

The mathematical models allow simulating the operation of a reactor under specific operating and design conditions, and identifying the parameters that have the greatest impact on the response variable. For the aerobic tank, the mass transport of both LCFA and oxygen was modeled. The critical parameters to promote the transport and oxidation of LCFA are: the interfacial area per unit volume and the proportion of degrading microorganisms of this chemical species that are found within them. From the results obtained, it can be concluded that the higher the number of flocs and the higher the proportion of cells capable of degrading LCFA, the lower the concentration of this chemical species in the effluent from the aerobic tank. Furthermore, it was observed that large flocs (with radii close to 55μm) with high cell content capable of consuming LCFA (volumetric fraction of 0.25) can consume higher amounts of this chemical species. The numerical simulations of the oxygen transport allows to affirm that there are operating conditions, according to the literature, that supply enough oxygen to maintain the viability of the aerobic microorganisms, and for the oxidation of the fatty substrate. The factors that have the greatest effect on oxygen transport and consumption in the aerobic reactor are the volumetric air flow and the maximum specific consumption rate of this substrate.

The analysis of the membrane tank did not lose sight of its coupled nature with the aerobic tank, using the results of the latter as a starting point. From the numerical simulations in space and in time of the membrane tank, it is concluded that the factors that influence transport of LCFA are summarized in the retentive capacity of the ultrafiltration membrane (by means of the Biot number) and the fluid velocity within the tank (reflected in the Péclet and Reynolds numbers). Regarding the retentive capacity of the membrane, there are two factors that determine its performance: First, the mass transport resistance between the liquid and the cassette and second, the mass transport resistances between the hollow fibers and the permeate. In practical applications, the former must be considerable so that the ultrafiltration cassettes retain most of the LCFA in the tank. While the second resistance must be lower to promote the reduction of the concentration of LCFA in the permeate.

Additionally, the 3D numerical simulations of the membrane tank allowed to reveal the main mechanisms by which the mass transport of LCFA is carried out. From the analysis of the total flux and the diffusive flux in the membrane tank, it is concluded that in most of the fluid external to the cassettes, mass transport is governed mainly by convection, while in the ultrafiltration cassettes the opposite occurs. The numerical simulations made it possible to predict the concentration of the chemical species at each point in the tank and at each time, as well as the concentration of LCFA in the permeate depending on the operating conditions and characteristics of the membrane. Under the operating conditions studied, the concentration in the permeate decreased up to 1.5-2% with respect to the feed concentration of the aerobic tank.

The mathematical models deduced here enabled the determination of the best design and operating conditions for the aerobic and membrane tanks in terms of dimensionless numbers and parameters. It is possible to obtain dimensional values that satisfy what was found in this parametric analysis by using the definitions given in previous sections for the aerobic and membrane tank. In this way, these parameters and dimensionless numbers can be used for any type of aerobic tank that meets the model assumptions detailed previously. The results presented in this work are useful for future experimental work, both for the design and for the improvement of existing membrane bioreactors.

As a matter of perspectives, it remains necessary to experimentally validate the models derived here in order to assess the validity of the assumptions that support them. Moreover, it is essential to evaluate the scope of the equilibrium models. Also, it is pertinent to further evaluate the integration of the membrane fouling phenomena in the ultrafiltration cassettes. The latter could be accomplished by the consideration of superficial accumulation in the derivation of the effective-medium model, or through reversible adsorption reactions at the boundary of this region and not only in the interfacial transport coefficients as done here. These and other relevant subjects shall be investigated in future studies.

Nomenclature

$a_{\sigma j}$	Interfacial areas per unit volume for the boundaries between the σ and the j zones ($j=\beta,\eta$), m^{-1}
A_{ij}	Superficial area between the i and the j zones ($i, j=\gamma,\eta,\kappa,\beta,\sigma$, $k\neq l$), m^2
$\mathscr{A}_j$	Surface of the averaging domain of the j-zone ($j=\gamma,\eta,\sigma$)
$\mathscr{A}_{kl}$	Boundary between the k and the l zones ($k,l=\gamma,\eta,\kappa,\beta,\sigma$, $k\neq l$)
$\mathbf{b}_j$	Closure variable that maps the influence of $\mathbf{I}\cdot\nabla\langle c_A\rangle$ into $\tilde{c}_{Aj}$ ($j=\beta,\eta,\sigma$), m
Bi_{ij}	Biot number for species i ($i=A,B$) between the η and the ωj regions
$Bi_{\gamma\eta}$	Biot number for species B at the boundary between the γ and the η-zones
$Bi_{\eta\zeta}$	Biot number for species A at the boundary between the η and the ζ regions
$Bi_{\zeta o}$	Biot number for species A at the boundary between the ζ-region and the permeate
c_i^k	Intrinsic average concentration of species i ($i=A,B$) in the k-region ($k=\beta,\sigma,\zeta$), mol/m^3
$c_{A\eta e}$	Molar concentration of species A in the η-region inlet of the aerobic tank, mol/m^3
$c_{B\gamma d}$	Molar concentration of species B in the γ-phase inlet (diffusers), mol/m^3
$\langle c\rangle$	Local averaged concentration, mol/m^3
$\mathbf{d}_{ij}$	Closure variable that maps the influence of $\frac{1}{\mu_j}\cdot\nabla\langle\mathscr{P}_j\rangle^j$ into $\widetilde{\mathscr{P}_j}$ ($i,j=\beta,\gamma,\eta,\sigma$)
D_{ij}	Effective diffusion coefficient of species i ($i=A,B$) in the ωj-region, m^2/s
D_{eff}	Total dispersion tensor of species A in the ζ-region, m^2/s
D_{ij}	Closure variable that maps the influence of $\frac{1}{\mu_j}\cdot\nabla\langle\mathscr{P}_j\rangle^j$ into $\mathbf{v}_j$ ($i,j=\beta,\gamma,\eta,\sigma$)
D^*	Total dispersion tensor for species A, m^2/s
D_A^*	Ratio between the effective diffusivity and the molecular diffusion coefficients for species A
$\mathscr{D}_{Aj}$	Molecular diffusivity of species A in the j-zone ($j=\eta,\beta$), m^2/s
H_{ij}	Relative apparent permeability tensor of the i-zone in the j-zone ($i,j=\beta,\gamma,\eta,\sigma$), m^2
H	Total apparent permeability tensor, m^2

$k^{\gamma\eta}$	Interfacial oxygen mass transport coefficient at the $\gamma\eta$ boundary, m/s
$k_{\lambda\eta}$	Hydrolysis reaction constant at the boundary between the λ and the η zones, m/s
$k_{\sigma j}$	Interfacial mass transport coefficient given for species A at the boundary between the j and the σ zones ($j = \eta,\beta$), m/s
$k_{ij}^{\eta\omega}$	Interfacial mass transport coefficient of species i ($i = A,B$) between the η and the ωj zones, m/s
k^{o}	Interfacial mass transport coefficient at the boundary between the ζ-region and the permeate, m/s
k^{ζ}	Interfacial mass transport coefficient at the boundary between the η and the ζ regions, m/s
K_{ij}	Thermodynamic equilibrium constant that relates the concentration of species i ($i = A,B$) between the extracellular matrix and the P_i-region
ℓ_j	Characteristic length of the j-zones ($i = \beta,\eta,\sigma$), m
$\mathbf{l}_i$	Unit cell vector in the i direction ($i = 1,2,3$), m
$\mathbf{n}_{ij}$	Unit normal vector directed from the i-zone to the j-zone ($i,j = \gamma,\eta,\lambda,\omega,\beta,\sigma,\ i \neq j$)
N_f	Number of floc sizes
P_i	Region composed of species i consuming cells
Pe	Péclet number
$\mathscr{P}_j$	Dynamic pressure in the j-zone ($j = \gamma,\eta,\beta$), kg/m s^2
$\mathscr{P}^{\sigma}$	Intrinsic average of the dynamic pressure in the β-phase inside the σ-region, kg/m s^2
$\langle \mathscr{P} \rangle$	Local averaged dynamic pressure, kg/m s^2
$\langle \mathscr{P}_j \rangle^j$	Intrinsic average of the dynamic pressure of the j-zone ($j = \gamma,\eta,\beta$), kg/m s^2
$\widetilde{\mathscr{P}_j}$	Spatial deviations of the dynamic pressure in the j-zone ($j = \gamma,\eta,\beta$), kg/m s^2
$\dot{Q}_{i\eta}$	Volumetric flow rate in the inlet of the η-region, m^3/s
$\dot{Q}_{d\gamma}$	Volumetric flow rate in the inlet of the γ-phase through the diffusers, m^3/s
$\dot{Q}_{o\eta}$	Volumetric flow rate in the outlet of the η-region, m^3/s
$\dot{Q}_{sup\gamma}$	Volumetric flow rate in the outlet of the γ-phase through the upper surface of the liquid in the tank, m^3/s
$\mathbf{r}_j$	Position vector that localizes points of the j-region ($j = \gamma,\eta,\beta,\sigma$), m

R_f	Maximum floc radius, m
Re	Reynolds number for the η-region of the membrane tank
Re_c	Reynolds number for the ζ-region
s_j	Closure variable that maps the influence of $\langle c_A \rangle$ into $\tilde{c}_{Aj}$ ($j = \beta,\eta,\sigma$)
t^*	Dimensionless time for species A in the membrane tank
t_i^*	Dimensionless time for species i ($i = A,B$) in the aerobic tank
t_D	Characteristic diffusion time for species A in the membrane tank, s
t_{D_i}	Characteristic diffusion time for species i ($i = A,B$) in the aerobic tank, s
$\mathbf{v}_{eff}$	Effective velocity vector in the ζ-region, m/s
$\mathbf{v}_j$	j-zone velocity ($j = \gamma,\eta,\omega,\beta$), m/s
$\mathbf{v}_{ij}$	Velocity of species i ($i = A,B$) in the j-zone, m/s
$\mathbf{v}^{\sigma}$	Intrinsic average of the velocity of the β-phase inside the σ-region, m/s
$\langle \mathbf{v} \rangle$	Superficial average velocity, m/s
V_j	Volume of the averaging domain of the j-zone ($j = \gamma,\eta,\omega,\sigma$), m^3
$\mathscr{V}_j$	Averaging domain of the j-zone ($j = \gamma,\eta,\omega$)
$\mathbf{w}_{ij}$	Speed of displacement of the boundary between the i-zone and the j-zone, $i,j = \eta,\gamma,\lambda,\omega,\ i \neq j$, m/s

Greek symbols

α	Jump coefficient that takes into account the transition from flow in a free-fluid zone and into a porous medium.
α_{P_i}	Half-saturation constant of species i consuming cells ($i = A,B$), mol/m^3
δ_{jA}	Kronecker delta
ε_{ej}	Volumetric fraction of the extracellular region that corresponds to species i ($i = A,B$) consuming cells in the ωj-region
$\varepsilon_{P_{ij}}$	Volumetric fraction of the P_i region ($i = A,B$) in the ωj-region
μ	j-zone viscosity ($j = \eta,\sigma,\beta$), kg m/s
μ_{ij}	Maximum specific consumption rate of species i ($i = A,B$) in the ωj-region, mol/m^{3}s
μ_{γ}	γ-phase viscosity, kg m/s
μ_{av}	Average viscosity, kg m/s
ρ_j	j-zone density ($j = \eta,\gamma,\beta$), kg/m^3
$\phi_{\lambda\eta}^2$	Thiele modulus at the boundary between the λ and the η zones

Acknowledgements

Sánchez-Vargas is thankful to Consejo Nacional de Ciencia y Tecnología (CONACYT) for providing her M.Sc. scholarship (No. 728330).

References

Acharya, C., Nakhla, G., & Bassi, A. (2006a, feb). A novel two-stage MBR denitrification process for the treatment of high strength pet food wastewater. *Journal of Hazardous Materials*, *129*(1-3), 194–203. doi: 10.1016/j.jhazmat.2005.08.039

Acharya, C., Nakhla, G., & Bassi, A. (2006b). Operational optimization and mass balances in a two-stage MBR treating high strength pet food wastewater. *Journal of Environmental Engineering*, *132*(7), 810–817.

Acharya, C., Nakhla, G., Bassi, A., & Kurian, R. (2006, jul). Treatment of high-strength pet food wastewater using two-stage membrane bioreactors. *Water Environment Research*, *78*(7), 661–670. doi: 10.2175/106143006x99812

Asif, M. B., Hai, F. I., Jegatheesan, V., Price, W. E., Nghiem, L. D., & Yamamoto, K. (2019). Applications of membrane bioreactors in biotechnology processes. In *Current trends and future developments on (bio-) membranes* (pp. 223–257). Elsevier. doi: 10.1016/b978-0-12-813606-5.00008-7

Beavers, G. S., & Joseph, D. D. (1967, oct). Boundary conditions at a naturally permeable wall. *Journal of Fluid Mechanics*, *30*(1), 197–207. doi: 10.1017/s0022112067001375

Becker, P., Abu-Reesh, I., Markossian, S., Antranikian, G., & Märkl, H. (1997, aug). Determination of the kinetic parameters during continuous cultivation of the lipase-producing thermophile bacillus sp. IHI-91 on olive oil. *Applied Microbiology and Biotechnology*, *48*(2), 184–190. doi: 10.1007/s002530051036

Bird, R. B., Stewart, W. E., & Lightfoot, E. N. (2002). *Transport phenomena* (second ed.). New York: John Wiley.

Brannock, M., Leslie, G., Wang, Y., & Buetehorn, S. (2010, January). Optimising mixing and nutrient removal in membrane bioreactors: CFD modelling and experimental validation. *Desalination*, *250*(2), 815–818. doi: 10.1016/j.desal.2008.11.048

Chai, Z., Lu, J., Shi, B., & Guo, Z. (2011, jun). Gas slippage effect on the permeability of circular cylinders in a square array. *International Journal of Heat and Mass Transfer*, *54*(13-14), 3009–3014. doi: 10.1016/j.ijheatmasstransfer.2011.02.049

Chu, C., & Lee, D. (2004a, apr). Multiscale structures of biological flocs. *Chemical Engineering Science*, *59*(8-9), 1875–1883. doi: 10.1016/j.ces.2004.01.040

Chu, C., & Lee, D. (2004b). Structural analysis of sludge flocs. *Advanced Powder Technology*, *15*(5), 515–532. doi: 10.1163/1568552042000246

d'Antonio, G., Esposito, G., Fabbricino, M., & Panico, A. (2016, may). Modelling the biological processes of MBR treatment plants. *Desalination and Water Treatment*, *57*(48-49), 22960–22967. doi: 10.1080/19443994.2016.1180477

Das, T., Bandopadhyay, A., Parthasarathy, R., & Kumar, R. (1985). Gas - liquid interfacial area in stirred vessels: The effect of an immiscible liquid phase. *Chemical Engineering Science*, *40*(2), 209–214. doi: 10.1016/0009-2509(85)80060-9

Delgado, S., Villarroel, R., Gonzalez, E., & Morales, M. (2011, sep). Aerobic membrane bioreactor for wastewater treatment – Performance under substrate-limited conditions. In *Biomass - detection, production and usage* (pp. 265–288). InTech. doi: 10.5772/17409

de los Santos-Sánchez, R., Valdés-Parada, F. J., & Chirino, Y. I. (2016, mar). Upscaling diffusion and reaction processes in multicellular systems considering different cell populations. *Chemical Engineering Science*, *142*, 144–164. doi: 10.1016/j.ces.2015.11.031

Ding, S., Liu, L., & Xu, J. (2013). A study of the determination of dimensionless number and its influence on the performance of a combination wastewater reactor. *Procedia Environmental Sciences*, *18*, 579–584. doi: 10.1016/j.proenv.2013.04.078

Farahani, M. H. D. A., Rabiee, H., Vatanpour, V., & Borghei, S. M. (2015, may). Fouling reduction of emulsion polyvinylchloride ultrafiltration membranes blended by PEG:

The effect of additive concentration and coagulation bath temperature. *Desalination and Water Treatment*, *57*(26), 11931–11944. doi: 10.1080/19443994.2015.1048739

Fenu, A., Guglielmi, G., Jimenez, J., Spèrandio, M., Saroj, D., Lesjean, B., ... Nopens, I. (2010, aug). Activated sludge model (ASM) based modelling of membrane bioreactor (MBR) processes: A critical review with special regard to MBR specificities. *Water Research*, *44*(15), 4272-4294. doi: 10.1016/j.watres.2010.06.007

Garcia-Ochoa, F., Gomez, E., Santos, V. E., & Merchuk, J. C. (2010, may). Oxygen uptake rate in microbial processes: An overview. *Biochemical Engineering Journal*, *49*(3), 289–307. doi: 10.1016/j.bej.2010.01.011

GE. (2014). Operation & maintenance manual, proyect: U-500615 [Computer software manual].

Gray, W. G. (1975, feb). A derivation of the equations for multi-phase transport. *Chemical Engineering Science*, *30*(2), 229–233. doi: 10.1016/0009-2509(75)80010-8

Gray, W. G., & Gray, G. A. (2017). *Introduction to environmental modeling*. Cambridge University Press. Retrieved from `https://www.ebook.de/de/product/27056737/william_g_gray_genetha_a_gray_introduction_to_environmental_modeling.html`

Hamedi, H., Ehteshami, M., Mirbagheri, S. A., Rasouli, S. A., & Zendehboudi, S. (2019). Current status and future prospects of membrane bioreactors (MBRs) and fouling phenomena: A systematic review. *The Canadian Journal of Chemical Engineering*, *97*(1), 32–58. doi: 10.1002/cjce.23345

Hauduc, H., Rieger, L., Oehmen, A., van Loosdrecht, M., Comeau, Y., Héduit, A., ... Gillot, S. (2012, sep). Critical review of activated sludge modeling: State of process knowledge, modeling concepts, and limitations. *Biotechnology and Bioengineering*, *110*(1), 24–46. doi: 10.1002/bit.24624

Henze, M., Grady, C., Gujer, W., Marais, G., & Matsuo, T. (1987, may). A general model for single-sludge wastewater treatment systems. *Water Research*, *21*(5), 505–515. doi: 10.1016/0043-1354(87)90058-3

Howes, F. A., & Whitaker, S. (1985). The spatial averaging theorem revisited. *Chemical Engineering Science*, *40*(8), 1387–1392.

Hsu, T.-C., Hanaki, K., & Matsumoto, J. (1983, jul). Kinetics of hydrolysis, oxidation, and adsorption during olive oil degradation by activated sludge. *Biotechnology and Bioengineering*, *25*(7), 1829–1839. doi: 10.1002/bit.260250712

Hu, H. H. (2012). Computational Fluid Dynamics. In *Fluid mechanics* (pp. 421–472). Elsevier. doi: 10.1016/b978-0-12-382100-3.10010-1

Janus, T., & Ulanicki, B. (2016, nov). Integrated benchmark simulation model of an immersed membrane bioreactor. *Process Safety and Environmental Protection*, *104*, 24–37. doi: 10.1016/j.psep.2016.08.005

Javed, S., Azeem, F., Hussain, S., Rasul, I., Siddique, M. H., Riaz, M., ... Nadeem, H. (2018, jan). Bacterial lipases: A review on purification and characterization. *Progress in Biophysics and Molecular Biology*, *132*, 23–34. doi: 10.1016/j.pbiomolbio.2017.07.014

Jeppsson, U. (1996). *Modelling aspects of wastewater treatment processes* (Unpublished doctoral dissertation). Lund Institute of Technology.

Ji, X., Chen, G., Zhang, Q., Lin, L., & Wei, Y. (2015, feb). Purification and characterization of an extracellular cold-adapted alkaline lipase produced by psychrotrophic bacterium *Yersinia enterocolitica* strain KM1. *Journal of Basic Microbiology*, *55*(6), 718–728. doi: 10.1002/jobm.201400730

Khakpour, S., Renzo, A. D., Curcio, E., Maio, F. P. D., Giorno, L., & Bartolo, L. D. (2017, dec). Oxygen transport in hollow fibre membrane bioreactors for hepatic 3D cell culture: A parametric study. *Journal of Membrane Science*, *544*, 312–322. doi: 10.1016/j.memsci.2017.09.024

Krzeminski, P., Leverette, L., Malamis, S., & Katsou, E. (2017, apr). Membrane bioreactors-A review on recent developments in energy reduction, fouling control, novel configurations, LCA and market prospects. *Journal of Membrane Science*, *527*, 207–227. doi: 10.1016/j.memsci.2016.12.010

Kurian, R., Acharya, C., Nakhla, G., & Bassi, A. (2005, nov). Conventional and thermophilic aerobic treatability of high strength oily pet food wastewater using membrane-coupled bioreactors. *Water Research*, *39*(18), 4299–4308. doi: 10.1016/j.watres.2005.08.030

Kurian, R., Nakhla, G., & Bassi, A. (2006, nov). Biodegradation kinetics of high strength oily pet food wastewater in a membrane-coupled bioreactor (MBR). *Chemosphere*, *65*(7), 1204–1211. doi: 10.1016/j.chemosphere.2006.03.050

Lasseux, D., Arani, A. A. A., & Ahmadi, A. (2011, jul). On the stationary macroscopic inertial effects for one phase flow in ordered and disordered porous media. *Physics of Fluids*, *23*(7), 073103. doi: 10.1063/1.3615514

Lee, Y., Cho, J., Seo, Y., Lee, J. W., & Ahn, K.-H. (2002, sep). Modeling of submerged membrane bioreactor process for wastewater treatment. *Desalination*, *146*(1-3), 451–457. doi: 10.1016/s0011-9164(02)00543-x

Liu, V. L., Nakhla, G., & Bassi, A. (2004, aug). Treatability and kinetics studies of mesophilic aerobic biodegradation of high oil and grease pet food wastewater. *Journal of Hazardous Materials*, *112*(1-2), 87–94. doi: 10.1016/j.jhazmat.2004.04.007

Liu, V. L., Nakhla, G., Bassi, A., & Al-Sabawi, M. (2003). Comparative evaluation of aerobic and anaerobic treatment of high oil and grease rendering wastewater. *Proceedings of the Water Environment Federation*, *10*, 157–169.

Lu, S., Imai, T., Ukita, M., Sekine, M., Higuchi, T., & Fukagawa, M. (2001, jun). A model for membrane bioreactor process based on the concept of formation and degradation of soluble microbial products. *Water Research*, *35*(8), 2038–2048. doi: 10.1016/s0043-1354(00)00461-9

Maere, T., Verrecht, B., Moerenhout, S., Judd, S., & Nopens, I. (2011, mar). BSM-MBR: A benchmark simulation model to compare control and operational strategies for membrane bioreactors. *Water Research*, *45*(6), 2181–2190. doi: 10.1016/j.watres.2011.01.006

Mannina, G., Cosenza, A., & Ekama, G. A. (2018, feb). A comprehensive integrated membrane bioreactor model for greenhouse gas emissions. *Chemical Engineering Journal*, *334*, 1563–1572. doi: 10.1016/j.cej.2017.11.061

Mines, R. O. (2019, nov). Oxygen transfer parameters and oxygen uptake rates revisited. *Journal of Environmental Science and Health, Part A*, *55*(4), 345–353. doi: 10.1080/10934529.2019.1694817

Moilanen, P., Laakkonen, M., & Aittamaa, J. (2005). Modelling fermenters with CFD. *Computer Aided Chemical Engineering*, *20*, 709–714. doi: 10.1016/s1570-7946(05)80240-8

Morgenroth, E., Arvin, E., & Vanrolleghem, P. (2002). The use of mathematical models in teaching wastewatertreatment engineering. *Water Science and Technology*, *45*(6), 229–233. doi: 10.2166/wst.2002.0110

Nakhla, G., Al-Sabawi, M., Bassi, A., & Liu, V. (2003, aug). Anaerobic treatability of high oil and grease rendering wastewater. *Journal of Hazardous Materials*, *102*(2-3), 243–255. doi: 10.1016/s0304-3894(03)00210-3

Nakhla, G., Liu, V., & Bassi, A. (2006, jan). Kinetic modeling of aerobic biodegradation of high oil and grease rendering wastewater. *Bioresource Technology*, *97*(1), 131–139. doi: 10.1016/j.biortech.2005.02.003

Rayleigh, L. (1892, dec). LVI. On the influence of obstacles arranged in rectangular order upon the properties of a medium. *The London, Edinburgh, and Dublin Philosophical Magazine and Journal of Science*, *34*(211), 481–502. doi: 10.1080/14786449208620364

Rittmann, B. E., Boltz, J. P., Brockmann, D., Daigger, G. T., Morgenroth, E., Sørensen, K. H., ... Vanrolleghem, P. A. (2018, jan). A framework for good biofilm reactor modeling practice (GBRMP). *Water Science and Technology*, *77*(5), 1149–1164. doi: 10.2166/wst.2018.021

Saalbach, J., & Hunze, M. (2008, apr). Flow structures in MBR-tanks. *Water Science and Technology*, *57*(5), 699–705. doi: 10.2166/wst.2008.122

SEMARNAT. (2018). Proy- nom-001-semarnat-2017, que establece los límites máximos permisibles de contaminantes en las descargas de aguas residuales en cuerpos receptores propiedad de la nación. [Computer software manual].

Shen, L.-G., Lei, Q., Chen, J.-R., Hong, H.-C., He, Y.-M., & Lin, H.-J. (2015, jun). Membrane fouling in a submerged membrane bioreactor: Impacts of floc size. *Chemical Engineering Journal*, *269*, 328–334. doi: 10.1016/j.cej.2015.02.002

Skoneczny, S., & Cioch, M. (2018, aug). Determination of steady-states in a tubular biofilm bioreactor with axial dispersion. *Chemical Engineering Research and Design*, *136*, 468–476. doi: 10.1016/j.cherd.2018.06.011

Spérandio, M., Masse, A., Espinosa-Bouchot, M., & Cabassud, C. (2005, nov). Characterization of sludge structure and activity in submerged membrane bioreactor. *Water Science and Technology*, *52*(10-11), 401–408. doi:

10.2166/wst.2005.0717

Takács, I., Dold, P., Morgenroth, E., Boltz, J., Schraa, O., Belia, E., ... Comeau, Y. (2011). Nutrient removal-manual of practice no. 34. In (p. 356-–486). Water Environment Federation, McGraw-Hill.

Tenore, A., Vieira, J., Frunzo, L., Luongo, V., & Fabbricino, M. (2018, dec). Calibration and validation of an activated sludge model for membrane bioreactor wastewater treatment plants. *Environmental Technology*, *41*(15), 1923–1936. doi: 10.1080/09593330.2018.1551940

Valdés-Parada, F., Alvarez-Ramirez, J., & Ochoa-Tapia, J. (2005, oct). An approximate solution for a transient two-phase stirred tank bioreactor with nonlinear kinetics. *Biotechnology Progress*, *21*(5), 1420–1428. doi: 10.1021/bp050110f

Valdés Parada, F. J. (2014). *Breviario sobre modelado matemático*. Universidad Autónoma Metropolitana. doi: 10.13140/2.1.2823.8400

Villadsen, J. (2016). *Fundamental bioengineering*. Singapore: John Wiley and Sons, Inc.

Wang, S.-J., & Zhong, J.-J. (2007). Bioreactor engineering. In *Bioprocessing for value-added products from renewable resources* (pp. 131–161). Elsevier. doi: 10.1016/b978-044452114-9/50007-4

Whitaker, S. (1996, oct). The Forchheimer equation: A theoretical development. *Transport in Porous Media*, *25*(1), 27–61. doi: 10.1007/bf00141261

Whitaker, S. (1999). *The method of volume averaging*. Dordrecht: Springer Netherlands.

Wood, B. D., & Whitaker, S. (2000, sep). Multi-species diffusion and reaction in biofilms and cellular media. *Chemical Engineering Science*, *55*(17), 3397–3418. doi: 10.1016/s0009-2509(99)00572-2

Wu, J., He, C., & Zhang, Y. (2012, apr). Modeling membrane fouling in a submerged membrane bioreactor by considering the role of solid, colloidal and soluble components. *Journal of Membrane Science*, *397-398*, 102–111. doi: 10.1016/j.memsci.2012.01.026

Xiao, K., Liang, S., Wang, X., Chen, C., & Huang, X. (2019, jan). Current state and challenges of full-scale membrane bioreactor applications: A critical review. *Bioresource Technology*, *271*, 473–481. doi: 10.1016/j.biortech.2018.09.061

Xiea, S., I.Haia, F., Zhanb, X., Guoc, W., Ngoc, H. H., Pricea, W. E., & Nghiem, L. D. (2016). Anaerobic co-digestion: A critical review of mathematical modelling for performance optimization. *Bioresource Technology*, *222*, 498–512. doi: 10.1016/j.biortech.2016.10.015

Zarragoitia-González, A., Schetrite, S., Alliet, M., Jáuregui-Haza, U., & Albasi, C. (2008, December). Modelling of submerged membrane bioreactor: Conceptual study about link between activated slugde biokinetics, aeration and fouling process. *Journal of Membrane Science*, *325*(2), 612–624. doi: 10.1016/j.memsci.2008.08.037

Zheng, Q.-Z., Wang, P., Yang, Y.-N., & Cui, D.-J. (2006, dec). The relationship between porosity and kinetics parameter of membrane formation in PSF ultrafiltration membrane. *Journal of Membrane Science*, *286*(1-2), 7–11. doi: 10.1016/j.memsci.2006.09.033